



The synergy of morphology and mixing state on the absorption of coated black carbon soot

Johannes Heuser^{1,2,a,*}, Claudia Di Biagio^{2,*}, Jérôme Yon³, Mathieu Cazaunau¹, Antonin Bergé^{2,b}, Edouard Pangui¹, Marco Zanatta^{1,4}, Laura Renzi⁴, Angela Marinoni⁴, Chenjie Yu², Servanne Chevaillier¹, Daniel Ferry⁵, Paolo Laj^{6,c}, Michel Maillé¹, Paola Formenti², Benedicte Picquet-Varrault¹, and Jean-Francois Doussin¹

¹ Univ Paris Est Creteil and Université Paris Cité, CNRS, LISA, F-94010 Créteil, France

² Université Paris Cité and Univ Paris Est Creteil, CNRS, LISA, F-75013 Paris, France

³ INSA Rouen Normandie, Univ. Rouen Normandie, CNRS, Normandie Univ., CORIA UMR 6614, 76000, Rouen France

⁴ Institute of Atmospheric Sciences and Climate, National Research Council of Italy, Bologna, Italy

⁵ Aix Marseille Univ., CNRS, CINaM, Marseille, France

⁶ Univ. Grenoble Alpes, IRD, CNRS, INRAE, Grenoble INP, IGE, 38000 Grenoble, France

^a now at : Deutscher Wetterdienst, Frahmredder 95, D-22393 Hamburg, Germany

^b now at : Laboratoire des Sciences du Climat et de l'Environnement, CEA–CNRS–UVSQ, IPSL, Université Paris-Saclay, 91191 Gif-sur-Yvette, France

^c now at: World Meteorological Organization, Geneva, Switzerland

*Corresponding author. Email: hannes.heu@gmail.com & claudia.dibiagio@lisa.ipsl.fr

Abstract

Black carbon (BC) strongly absorbs light and contributes to climate warming. Coating formation on fractal BC-containing soot is a ubiquitous atmospheric process that enhances its absorption, but the extent of this absorption enhancement (E_{abs}) remains uncertain and difficult to represent in models. In this study, we use large simulation chamber experiments to investigate BC absorption and its modification by coating formation and ageing. Polydisperse fractal BC-containing soot was mixed with non-absorbing atmospherically-relevant secondary aerosols (sulfuric acid and α -pinene secondary organic aerosols). Varying reaction dynamics produced different coating rates and masses, mimicking atmospheric processing. The evolution of soot and coating properties was tracked for up to 20 hours. The results of this study suggest a general positive correlation between E_{abs} and coating amount on soot. However, they also experimentally demonstrate the strong effect of morphological modifications and mixing state heterogeneity on BC absorption, both depending on the reaction dynamics of coating formation and ageing of the coated soot. Combined variations in morphology and mixing state affect the magnitude of E_{abs} and its further evolution, leading, depending on processing, to either an increase or decrease in absorption. The range of measured E_{abs} resulting from soot processing cannot be reliably predicted using a fixed E_{abs} value or by a core-shell optical model, two approximations commonly used in climate models. These results support the need for new formalisms that would take into account both morphological and mixing state heterogeneity to improve model predictions of BC absorption and its role on the radiative budget.



35 **1 Introduction**

Black carbon (BC) is the major aerosol light-absorber and one of the strongest contributors to modern climate forcing (Bond et al., 2013; Intergovernmental Panel on Climate Change (IPCC), 2023; Lee et al., 2021). Soot, as the most common BC-containing aerosol, is emitted as a product of incomplete combustion of biomass, biofuels, and fossil fuels, and displays a broad atmospheric distribution ranging from the surface into the stratosphere and from urban environments to remote locations (Bond et al., 2013; Liu et al., 2020; Schwarz et al., 2006). Light absorption by BC in soot is strongly affected by internal mixing with brown carbon (Cheng et al., 2019; Heuser et al., 2025) and secondary species (Colbeck et al., 1990; Schnaiter et al., 2005; Wang et al., 2017; Zhang et al., 2018), either co-emitted or formed during atmospheric lifetime. In particular, the formation of a non- or weakly-absorbing coating on soot has been established to enhance its absorption due to refracting and reflecting effects (Bond and Bergstrom, 2006; Cappa et al., 2012a, 2019; Fuller et al., 1999). This enhancement is commonly expressed via the enhancement factor E_{abs} , which is the ratio between the absorption of the coated and the uncoated soot.

Currently, the magnitude and dependencies of E_{abs} on coating and soot properties remain controversial (Cappa et al., 2012b; Fierce et al., 2016, 2020; Liu et al., 2017; Peng et al., 2016). Most studies generally describe an increasing E_{abs} with an increasing coating-to-soot or coating-to-BC mass ratio. Laboratory works retrieved E_{abs} values as high as 2 for internally mixed soot with varying coating-to-BC mass ratios (Cappa et al., 2012b; Lack et al., 2009; Peng et al., 2016; Schnaiter et al., 2005). Field observations led to diverse results, with some studies reporting E_{abs} up to 3 (Liu et al., 2015, 2017; Zhang et al., 2018), while others calculate small E_{abs} despite large coating masses (Cappa et al., 2012b, 2019; Chan et al., 2010; Healy et al., 2015). The spread of observations suggests that the mechanisms leading to absorption enhancement do not depend solely on the amount of coating mass deposited on the BC. Key aspects evidenced to affect E_{abs} magnitude and variability include (i) the single particle properties and mixing state including the morphological organization of the soot and its coating (Chen et al., 2024; Liu et al., 2017; Sedlacek III et al., 2012), i.e. the way secondary species distributes over the fractal soot including void filling or encapsulating soot with consequent collapse of the aggregate; (ii) the diversity in the particle-to-particle mixing state in the soot population (Cappa et al., 2019; Fierce et al., 2020; Wang et al., 2023; Zeng et al., 2024), and the (iii) rate of coating formation and ageing (Cappa et al., 2019; Peng et al., 2016). Despite advances in identifying the various mechanisms contributing to the variability of soot absorption, including evaluation of instrumental and methodological uncertainties (Asmi et al., 2025), the process-level understanding of the impact of ageing on E_{abs} remains elusive.

As a consequence of this lack of knowledge, and despite the evident variability, most climate models keep an oversimplified estimation of E_{abs} either via a concentric core-shell optical model (the Mie core-shell for spherical coated particles) or a fixed E_{abs} factor, often set at the value of 1.5 (Sand et al., 2021). However, both approximations are identified to overestimate E_{abs} (Cappa et al., 2019; Fierce et al., 2020; Liu et al., 2017; Wang et al., 2023).

In order to advance towards a mechanistic understanding of E_{abs} , in this work, we investigate the absorption of BC and its modification due to coating formation based on systematic laboratory experiments in a large simulation chamber. We generated polydisperse fractal BC-containing soot and mixed it with non-absorbing atmospherically-relevant secondary aerosol species (sulfuric acid, H_2SO_4 , and α -pinene secondary organic aerosols, SOA). Multiple coating experiments were performed with varying reaction dynamics, leading to slower/faster and lower/higher coating mass formation, mimicking the processing occurring in the



70 atmosphere. The evolution of the soot and coating properties over up to 20 hours of chamber lifetime was studied to evaluate the E_{abs} magnitude and variability, and its link to physico-chemical properties.

2 Methods

This study utilises the 4.2 m³ stainless steel CESAM atmospheric simulation chamber (French acronym for Experimental Multiphase Atmospheric Simulation Chamber) (Doussin et al., 2023; Wang et al., 2011) (<https://cesam.cnrs.fr/>, last access: 31
75 March 2026). CESAM is a temperature-, pressure-, and humidity-controlled chamber designed to allow multiphase atmospheric (photo-) chemistry, widely used to investigate the formation, evolution and climate-relevant properties of primary and secondary sub- and super-micron aerosols (Baldo et al., 2020, 2023; Battaglia et al., 2025; Caponi et al., 2017; De Haan et al., 2023; Di Biagio et al., 2017, 2019, 2023; Heuser et al., 2025). The gaseous and aerosol content can be varied in CESAM to reproduce atmospherically-relevant mixtures under varying particles and gas-phase concentrations. Realistic solar irradiation is provided by
80 three 6.5 kW Xenon arc lamps. A stainless steel fan placed at the bottom of the reactor ensures the homogeneity within the volume, with a mixing time of around one minute. The aerosol lifetime in the chamber is between 6 to more than 24 hours for particles of diameter between 50 and 200 nm (Lamkaddam et al., 2017). CESAM is equipped with 12 circular flanges enabling the deployment of multiple instruments for online and offline measurements of the chamber's thermodynamic state, gas-phase composition, aerosol concentration and their physico-chemical and spectral optical properties.

85 A total of 16 experiments were performed to investigate the evolution of the soot optical properties due to different ageing conditions, as summarized in Table 1. Six of these experiments targeted the formation of a coating on soot under diverse reactions dynamics and its subsequent ageing. In three experiments, H₂SO₄ coating was generated via the reaction of SO₂ and hydroxyl radical (OH). In two of these experiments (H₂SO₄-high1, H₂SO₄-high2), O₃ (at concentration of about 950 ppb) was used for OH-radical production via photolysis in the presence of water vapour. An additional experiment (H₂SO₄-low) was performed without
90 active OH-production from O₃. In the other three coating experiments, SOA was generated via the ozonolysis of α -pinene. The quantities of α -pinene and soot were changed at similar O₃ concentration (306 to 384 ppb) to alter the amount of SOA and soot coating generated. In the SOA-S_{ref} experiment, the initial soot mass ($63 \pm 6 \mu\text{g m}^{-3}$) was comparable to H₂SO₄ experiments (within 80 and 90 $\mu\text{g m}^{-3}$). In SOA-S_{low} smaller quantities of soot ($\sim 13 \mu\text{g m}^{-3}$) were injected while α -pinene was kept comparable to SOA-S_{ref} (~ 60 ppb), and SOA_{high}-S_{high} was performed at about two to three times the soot and precursor concentration as SOA-S_{ref} (soot
95 $\sim 169 \mu\text{g m}^{-3}$, α -pinene ~ 120 ppb). Ten control experiments were performed to evaluate the impact on the soot properties of each compound, process, and protocol used in the coating experiments. These aimed to quantify the effects of soot lifetime and coagulation under dry and humid conditions, of irradiation under dry and humid conditions, and of the presence of O₃ and OH-radicals under humid conditions. Further control experiments were performed with submicron ammonium sulphate and sulphuric acid aerosols with the aim of validating the performances and consistency of optical and physico-chemical observations, as
100 presented and discussed in (Heuser et al., 2025).

2.1 Protocol of chamber experiments

For the experiments, the chamber was filled with an 80/20-mixture of N₂ (evaporated from liquid N₂; Messer, purity >99.995%) and O₂ (Linde 5.0, purity $\geq 99,999\%$) at a slight overpressure (ambient conditions +5 hPa) to avoid external contaminations.



105 **Table 1.** List of soot ageing experiments. These are separated into the coating experiments, in which coating generation was achieved and studied, and the control experiments. Table columns indicate: the experiment name, the measurement interval after coating formation, the total soot lifetime in the chamber, the initial soot mass concentration, the ozone (O₃) concentration at the start of the SOA generation, and the SO₂ and α -pinene injected concentrations. The list of digital object identifiers (DOI) for the experimental data are also reported. Those data are available through the Database of Atmospheric Simulation Chamber Studies (DASCS) of the EUROCHAMP Data Centre (<https://data.eurochamp.org/data-access/chamber-experiments/>) also available via the ACTRIS data portal (<https://data.actris.eu/>).

110

Experiment	Measurement interval for aged aerosol (hh:mm)	Total lifetime (hh:mm)	Initial mass concentration [$\mu\text{g m}^{-3}$]	RH (%)	O ₃ [ppb]	SO ₂ / α -pinene [ppb]	Dataset DOI
Coating experiments							
H ₂ SO ₄ -low	03:03	06:50	90 ± 8	~30	/	273 ± 2	https://doi.org/10.25326/76FN-TA55
H ₂ SO ₄ -high1	20:31	24:48	89 ± 9	~30	950 ± 5	260 ± 2	https://doi.org/10.25326/PWHP-ED62
H ₂ SO ₄ -high2	20:27	25:16	80 ± 8	~30	955 ± 6	258 ± 2	https://doi.org/10.25326/A18P-JF85
SOA-S _{ref}	20:01	24:43	63 ± 6	~30	384 ± 2	60 ± 16	https://doi.org/10.25326/AK6B-ZA08
SOA _{high} -S _{high}	21:58	27:03	169 ± 18	~30	306 ± 2	120 ± 12	https://doi.org/10.25326/N7S0-S115
SOA-S _{low}	02:03	07:22	13 ± 2	~30	354 ± 2	60 ± 16	https://doi.org/10.25326/BGRM-3554
Control experiments							
Soot coagulation dry 1	21:51	21:51	63 ± 6	/	/	/	https://doi.org/10.25326/8KVR-AA70
Soot coagulation dry 2	25:36	25:36	198 ± 18	/	/	/	https://doi.org/10.25326/M24W-V933
Soot irradiation dry 1	02:05	05:01	67 ± 6	/	/	/	https://doi.org/10.25326/2QRB-4E45
Soot irradiation dry 2	01:03	02:37	58 ± 6	/	/	/	https://doi.org/10.25326/8HT1-WA13
Soot coagulation humid	05:16	07:11	78 ± 8	~30	/	/	https://doi.org/10.25326/WN6E-0272
Soot irradiation humid	04:44	06:46	79 ± 8	~30	/	/	https://doi.org/10.25326/EAQE-VX80
Soot O ₃ irradiation humid 1	03:24	07:48	74 ± 7	~30	928 ± 5	/	https://doi.org/10.25326/JRAC-4W36
Soot O ₃ irradiation humid 2	02:31	06:03	/	~30	925 ± 5	/	https://doi.org/10.25326/2BD3-Q151
Soot O ₃ irradiation humid 3	03:11	07:59	/	~30	992 ± 6	/	https://doi.org/10.25326/9G66-MG61
Soot O ₃ irradiation humid 4	02:04	05:31	/	~30	1003 ± 6	/	https://doi.org/10.25326/XJKP-JD08

115 The combustion aerosol was produced with a miniCAST propane-diffusion flame soot generator (Model 6204 Type C, Jing Ltd., Switzerland), which allows for repeatable soot generations (Heuser et al., 2025; Moore et al., 2014). For all experiments, the propane, mixing N₂, quench N₂, oxidation, and dilution air flows were kept at 0.03, 0, 2, 0.75, and 5 L min⁻¹, respectively, as corresponding to the first operation point of the miniCAST, producing a fuel-lean combustion with a global equivalence ratio of 0.91. The bulk elemental-to-total carbon ratio (EC/TC) of the generated cast soot (CS), hereafter referred to as CS1, was measured at 0.79 ± 0.11, indicating a BC-dominated composition (Heuser et al., 2025). The CS1 was injected into CESAM through an activated carbon denuder for a duration between 30 and 390 seconds, depending on the targeted mass concentration.

120 The water vapour was injected about 2 hours after the soot to reach a relative humidity of ca. 30%, as steam from a modified pressure cooker filled with ultra-pure water (18.2 M Ω , 3.2ppb TOC, Milipak) (Wang et al., 2011). Ozone was injected directly out of an ozone generator (BMT 802N, BMT MESSTECHNIK GMBH), using bottled O₂ (Linde 5.0, purity ≥ 99,999%). About 40 ppb of Butanol-d₉ (1-Butanol D₉, 98%, Euroisotop) was volatilized and injected, prior to the O₃, using a vacuum line and a glass bulb. The Butanol-d₉ was used as a tracer to monitor the OH-exposure. Following O₃, about 75 to 90 minutes later, the precursors for the secondary aerosol and coating formation were introduced in the chamber volume. The SO₂ (Merck, 99.95%) was injected using a calibrated gas-tight syringe and septum inlets. The H₂SO₄ generation itself was then started by initiating the photochemical hydroxyl radical production by turning on the three Xenon-arc lamps. The light of the lamps is introduced via quartz windows

125



equipped with Pyrex® filters (6.5mm), generating a spectrum close to solar radiation at ground level (Wang et al., 2011). Temperature fluctuations due to the radiation were limited with a cooling system (LAUDA Integral-T 10000 W) to about 1 to 2 K, resulting in a temperature range of 294 to 301 K during experiments. The α -pinene (98%, Sigma-Aldrich) was volatilized using a vacuum line, and a known quantity of the SOA precursor was injected with a glass bubble. Dark conditions and minimal temperature fluctuations between 289 and 291 K required no temperature regulations in the SOA experiments. After 3 hours since the start of secondary aerosol formation, the majority of the α -pinene was consumed (<3 ppb remaining), and the H₂SO₄ coating production was stopped by turning off the lamps. In experiments H₂SO₄-high1/2, SOA-S_{ref}, and SOA_{high}-S_{high}, the coated soot was left in suspension under dark conditions with reduced instrumentation and minimal dilution (about 3 L min⁻¹). After 15 hours, the aged soot was again fully characterized.

At the end of each experiment, the CESAM chamber was evacuated to around 3 10⁻⁴ hPa to avoid carryover contaminations and stays evacuated between subsequent experiments. The chamber was also additionally cleaned manually at the beginning of each campaign and when changing the chemical system. More details on the experimental protocol for the soot and control experiments are provided in Text S1 and Table S1 in the Supplementary information.

2.2 Measurements

A large complementary set of state-of-the-art instrumentation was used to characterize the physico-chemical and spectral optical properties of the soot aerosol, as well as the thermodynamic state of the volume and its gaseous content. The full instrumentation including measurement uncertainties are detailed in Tables S2 and S3, and previously described in Heuser et al. (2025). The majority of online measurements were performed continuously throughout experiments with the exception of short disconnections at soot and water vapour injections. During the 15h dark ageing, only the number size distribution was measured continuously. Air sampled out of the chamber during experiments (varying between 3 and 22 L min⁻¹) was compensated with a particle-free N₂/O₂-mixture, leading to a constant dilution of the compounds in the chamber. The main used instruments to characterise the aerosol properties in this work are presented in the following.

The aerosol number size concentration between 19.5 and 881.7 nm over 64 channels (dN/dlogD_m; D_m, mobility diameter) was continuously measured at 3-minute resolution with a scanning mobility particle sizer (SMPS, TSI, Krypton⁸⁵ neutraliser, DMA 3080, CPC 3772, with 2.0/0.2 L min⁻¹ sheath/aerosol flow rates). Measurements were corrected for diffusion losses and multiple charge effects with the instrument software. The number size distributions were fitted with log-normal functions to determine the population count (or number) median diameter (CMD).

The aerosol effective density (ρ_{eff}) was derived from measurements with a centrifugal particle mass analyzer (CPMA – Cambustion) and an SMPS (TSI, X-ray neutraliser 3087, DMA 3080, CPC 3775 high). A DMA-CPMA-CPC setup was used to measure the aerosol mass-resolved size distributions as described in Heuser et al. (2025) and Yon et al. (2015). Multiple measurements between 0.03 to 6 femtograms allowed for the calculation of the effective density over the range of soot diameters $\rho_{\text{eff}}(D_m)$ (Kasper, 1982; Park et al., 2003). A complete DMA-CPMA-CPC scan to derive a full $\rho_{\text{eff}}(D_m)$ curve lasted about 35 minutes. The scans were performed after soot injection in the chamber, after each compound injected in the chamber and for coated soot, before and after long-term ageing. The $\rho_{\text{eff}}(D_m)$ data were fitted with a power-law relation (Park et al., 2003)

$$\rho_{\text{eff}}(D_m) = aD_m^{D_{\text{fm}}-3}. \quad (1)$$



to determine the mass-mobility exponent (D_{fm}) and the pre-factor a . The D_{fm} is dependent on the morphology of the aerosols (it equals to 3 for spherical-void free particles, and is around 2.2 for soot (Maricq and Xu, 2004; Sorensen, 2011)) and, together with ρ_{eff} , was used as a proxy for morphological and chemical evolution of the soot over the simulated ageing processes (Park et al., 2003; Sorensen, 2011). The $\rho_{eff}(D_m)$ was used to determine the total aerosol mass concentration (m_{total}) as:

$$m_{total} = \sum_i \frac{\pi}{6} D_{m,i}^3 \frac{dN}{d\log D_{m,i}} d\log D_{m,i} \rho_{eff}(D_{m,i}) \quad (2)$$

where $\rho_{eff}(D_{m,i})$ indicates the values extrapolated at the D_m values of the SMPS and $dN/d\log D_m$ is the corresponding measured number size distribution (the subscript i in Eq. (2) indicates the SMPS channel). As discussed in Heuser et al. (2025), the m_{total} compared well with gravimetric measurements from a tapered element oscillating microbalance (TEOM 1400a – Thermo Scientific). Noteworthy, the mass concentration calculated with Eq. (2) lacks sensitivity to ongoing aerosol physico-chemical processing due to the coarse time resolution of ρ_{eff} measurements.

Morphological information of the soot particles were also retrieved using transmission electron microscopy (TEM). Soot particles samples were collected over different moments of the experiments using three TEM grids (200-mesh copper grid with a Formvar/carbon film, Agar Scientific) glued onto the Teflon-pore filters (47mm Nuclepore Whatman, 0.8 μm nominal pore size). Sampling was performed with a custom-made stainless-steel filter holder operated at a flow rate of 2-4 L min^{-1} . The total sampling time was adjusted to ensure similar area loadings between different samples. The TEM images were acquired with a JEOL® 100CXII and a JEOL® JEM2010 microscopes and processed using the same protocol as described in Heuser et al. (2025).

A single particle soot-photometer (SP2 – Droplet Measurement Technologies, 1-min resolution, (Stephens et al., 2003)) was used to measure the refractory mass concentration (m_{rBC}) and its size distribution between 89 and 567 nm (volume equivalent diameter, D_{ve}), assuming a material density of 1.8 g cm^{-3} . The SP2 was calibrated with fullerene and size- and mass-selected soot (Lorber et al., 2012). The measured size distributions from the SP2 were extrapolated based on a lognormal fit to approximate m_{rBC} over the full soot size range (Liu et al., 2014). The ratio of the SP2 fullerene-calibrated m_{rBC} to m_{total} (1.2-1.8) was determined for each experiment prior to the coating formation. This ratio was used to convert m_{rBC} into total soot mass (m_{soot}), enabling the tracking of soot mass concentration throughout the experiments.

Spectral optical properties were monitored with a nephelometer (TSI Model 3563 Integrating Nephelometer, 1-sec resolution, sampling flow rate 2 L min^{-1} , Anderson et al. (1996)), providing the scattering coefficient (b_{scat}) at 450, 550, and 700 nm, and two Cavity Attenuated Phase Shift monitors (CAPS PMex, (Kebabian et al., 2007; Massoli et al., 2010)) and two CAPS single scattering albedo monitors (CAPS PM_{SSA}, Onasch et al. (2015)) (Aerodyne Research, both operated at 1-sec resolution, sampling flow rate 0.85 L min^{-1}) measuring the extinction coefficient (b_{ext}) at 450 and 630 nm. The aerosol scattering coefficients measured at angles between 7° and 170° from the nephelometer were corrected based on Massoli et al. (2009) to obtain the fully integrated 0-180° b_{scat} by using a real refractive index of 1.95 (Bond and Bergstrom, 2006). The scattering Ångström exponent was calculated via the power-law fit of the spectral b_{scat} and used to interpolate the scattering coefficient at 630 nm. The aerosol absorption coefficient (b_{abs}) was determined from extinction-minus-scattering at 450 and 630 nm, and validated against reference filter-based measurements (Heuser et al., 2025).

The gas phase composition was measured during the experiments using a set of gas monitors measuring the concentrations of SO₂ (Horiba APSA370), O₃ (Horiba APOA370), NO_x/NO₂/NO (Horiba APNA370), NO₂ (Teledyne T500U), and CO/CO₂ (APEE – ProCees). To follow the content of α -pinene and butanol-D₉ compounds a Proton Transfer Reaction Time of Flight Mass



Spectrometer (PTR-ToF-MS, Kore Technology, Jordan et al. (2009)) was used. The atmospheric state of the chamber was tracked throughout the experiments by measurements of the pressure (Baratron type MKS 626AX13TDE (high range)/ 626AX11TDE (low range)), temperature, and relative humidity (Vaisala HMP234- Hygrometer).

2.3 Data analysis

2.3.1 Experimental evaluation of the absorption enhancement (E_{abs}) and coating-to-soot mass ratio ($M_{\text{R,bulk}}$)

Online data were averaged over common base time intervals of 3 minutes, a value about double the typical mixing time of the chamber, and all volumetric quantities were converted into standard pressure and temperature conditions (1013.25 mbar, 273.15 K).

The mass absorption cross section (MAC) of the soot particles was calculated at 450 and 630 nm at 3-minute resolution for each experiment as the ratio of the b_{abs} and m_{soot} . The uncertainty on the 3-min MAC was determined as the propagation of the uncertainty of b_{abs} ($\pm 10\text{-}30\%$) and m_{soot} ($\pm 26\%$) and averages at about 30%, increasing throughout each experiment with decreasing the number and mass aerosol concentration. The absorption enhancement factor E_{abs} was calculated at 450 and 630 nm and 3-min resolution as the ratio of the MAC prior to and after the coating generation ($E_{\text{abs}} = \text{MAC}_{\text{coated}} / \text{MAC}_{\text{prior}}$). The $\text{MAC}_{\text{prior}}$ was estimated for each experiment as the average MAC for the 60-90 minutes prior to the precursor injection and the start of the secondary aerosol generation. The uncertainty of E_{abs} , estimated with error propagation from the MAC values, was estimated on average at about 35%.

The measurements from the SMPS, CPMA and SP2 were combined to retrieve the bulk coating-to-soot mass ratio ($M_{\text{R,bulk}}$) at 3-min resolution during experiments. The $M_{\text{R,bulk}}$ is the ratio of the secondary aerosol mass deposited on the soot either due to condensation or coagulation ($m_{\text{deposited}}$) and the soot mass (m_{soot}) ($M_{\text{R,bulk}} = m_{\text{deposited}} / m_{\text{soot}}$). The $m_{\text{deposited}}$ was retrieved by subtracting the m_{soot} (as derived from SP2 measurements) and the mass of secondary aerosol resulting from nucleation (m_{nuc}) from m_{total} as:

$$m_{\text{deposited}} = m_{\text{total}} - m_{\text{soot}} - m_{\text{nuc}} \quad (3)$$

The m_{total} was determined from full integration of (Eq. 2), while the m_{nuc} was calculated by integrating Eq. (2) over the size range of nucleating secondary aerosol and using the corresponding effective density from CPMA measurements. For the coated aerosol the first size-resolved $\rho_{\text{eff}}(D_m)$ measurement was performed about 60 minutes after coating generation, i.e. for already significantly processed/coated soot, then repeated after 15h ageing. The $M_{\text{R,bulk}}$ is therefore the most reliable around these $\rho_{\text{eff}}(D_m)$ scans and beyond this point is an approximation that is only sensitive to significant coating evolution via size changes. To minimize bias and potential misinterpretation, the $M_{\text{R,bulk}}$ values were only considered after an initial processing period of 15 minutes, when most significant evolution in the coating experiments is expected. The uncertainty on $M_{\text{R,bulk}}$ was estimated as the propagation of the uncertainties of the individual masses and averages at around 50%, increasing, as for the MAC, throughout the experiments due to the dilution of the chamber volume.

2.3.2 Mie core-shell calculations of E_{abs} versus $M_{\text{R,bulk}}$

The E_{abs} was also theoretically calculated using the Mie-core-shell optical theory for varying $M_{\text{R,bulk}}$ to compare one of the most common modelling approaches with our measurements. In the Mie core-shell an aerosol particle is represented as a volume-



equivalent sphere coated with a homogeneous layer with a uniform thickness. This enables the representation of the coated particles via an inner diameter (core particle) and a total diameter (particle/core and coating/shell).

The Mie core-shell calculations were done by assuming that the soot particles have a homogeneous size-independent composition.

235 Additionally, a fixed reference soot number size distribution was chosen to represent the aerosol core, translated from mobility size to volume-equivalent size based on the $\rho_{\text{eff}}(D_m)$ measurements and the derived material density of the soot (Heuser et al., 2025).

The size distribution taken just prior to SO_2 injection during the H_2SO_4 -high1 experiment was chosen as a representative soot core distribution. The outer diameter due to coating formation on soot was determined using the densities of the soot, H_2SO_4 , and α -pinene SOA calculated from the measured $\rho_{\text{eff}}(D_m)$. Refractive indices for the core and the shell were taken from the literature and from CESAM experiments. For the core soot, two complex refractive index ($m=n-ik$) values were used at 450 and 630 nm: (i)

240 the most commonly assumed value for BC of 1.95-0.79i (Bond and Bergstrom, 2006) and (ii) a second value of 1.46-0.3i (Habib and Vervisch, 1988) selected to actively represent a value on the other end of the complex refractive index range generally associated with soot. For the H_2SO_4 coating, values of the complex refractive index were retrieved from control experiments described in Heuser et al. (2025), in which a value of 1.30-0i (450 nm) and 1.24-0i (630 nm) was found to best describe the H_2SO_4

245 generated in CESAM at 30% relative humidity. For the α -pinene SOA, a wavelength-independent real part of 1.5 with a negligible imaginary part was used based on previous studies (Denjean et al., 2015; Kim et al., 2010; Schnaiter et al., 2005).

To determine the E_{abs} at different $M_{\text{R,bulk}}$, the b_{abs} was calculated once for an uncoated aerosol using classical Mie theory and the size distribution of the soot core and then with Mie-core-shell for progressively increasing outer diameters for varying $M_{\text{R,bulk}}$ from 1 to 5 in 0.1 steps. The $E_{\text{abs}}(M_{\text{R,bulk}})$ was calculated as the ratio of the b_{abs} of the uncoated and coated soot for the given $M_{\text{R,bulk}}$.

250 3. Results

The time evolution of number size distribution, CMD, $M_{\text{R,bulk}}$, and E_{abs} at 630 nm, as well as TEM pictures for the fresh, coated, and aged soot particles for the H_2SO_4 and the α -pinene SOA coating experiments are shown in Fig. 1 and 2. Timelines for all the H_2SO_4 and SOA coating experiments, also including E_{abs} at 450 nm, are shown in Fig. S2-3, and S11-S16 of the supplementary information. The size-resolved $\rho_{\text{eff}}(D_m)$ measured for the different control and coating experiments is shown in Fig. 3. Table 2

255 synthesises the physico-chemical and optical properties of the fresh, coated and aged soot aerosols.

3.1 Pre-coating soot evolution and ageing control experiments

The start point for the experiments is an about two-hour-old soot aerosol for which a complete set of properties was measured to determine an initial reference. In its fresh state the investigated soot has a lacy fractal morphology, as shown in TEM images (Fig. 1e, 2e), quantified by a mass-mobility exponent D_{fm} of 2.11 ± 0.04 . The soot shows a mono-modal size distribution with an initial count median diameter CMD around 100-120 nm, increasing to values between 150 and 250 nm due to coagulation within the first

260 2 hours of experiments (Fig. 1a, 2a). For the CMD of 200 nm the fresh soot particles have an average ρ_{eff} of $232 \pm 13 \text{ kg m}^{-3}$ (Fig. 3). The soot mass concentration at the end of this characterisation and just prior to the water vapour injection ranges between 13 and $169 \text{ } \mu\text{g m}^{-3}$.

265 As shown in Fig. 1a and 2a, no significant changes in the CMD or number concentration are observed due to water vapour injection, with the exception of minimal loss of particles that can be attributed to a physical washout and the short pressure change



in the chamber. Similarly, no significant effect on the soot physico-chemical is observed due to ozone injection and the following 2-3 hours prior to the H₂SO₄ and SOA generation. Measurements of $\rho_{\text{eff}}(D_m)$ show only slight differences, within uncertainties, between pre-coating steps and fresh soot (Fig. 3), indicating no significant chemical or morphological changes. The MAC values show a consistent minor declining trend during the pre-coating steps, as indicated by the decrease of E_{abs} (Fig. 1d, 2d). This decrease remains however well inside one standard deviation of the MAC values of fresh soot. To account for this minor evolution, as described in Sect. 2.3.1, the reference $\text{MAC}_{\text{prior}}$ to calculate E_{abs} is taken by averaging values over the last undisturbed suspension period prior to the coating generation, corresponding to about 60 to 90 minutes.

No significant changes in the soot physico-chemical and optical properties are likewise observed for the control experiments for the various conditions tested. The effective density measurements (Fig. 3a) and the mobility exponents determined from them are found to be rather stable compared to the fresh soot and the pre-coating steps. The only experiments where D_{fm} shows some stronger deviation, with values around 1.96 ± 0.01 , are the long-term ageing experiments Soot coagulation dry 1 and 2. These deviations are however linked to measurement bias due to the very low aerosol concentrations after 24 hours of coagulation and dilution. The MAC values remain for all conditions inside one standard deviation of the values of fresh soot as reported in Heuser et al. (2025) (Fig. S1). Timelines and results of the ageing control experiments are shown in the supplementary information (Fig. S17-S25).

280

3.2 Soot-H₂SO₄ coating and ageing

As shown in Fig. 1a and 1b, the start of the H₂SO₄ generation leads to a progressive increase of soot CMD due to the condensation of coating material on the particles, reflected in a marked increase of the soot ρ_{eff} (Fig. 3b), as well as to the production of new modes associated with homogeneous particle formation below CMDs of 120 nm. The estimated H₂SO₄ mass deposited on the soot due to condensation; butv also coagulation with the H₂SO₄ mode, is quantified via the bulk coating-to-soot mass ratio $M_{\text{R,bulk}}$ (Fig. 1c). The H₂SO₄-low condition (lower OH oxidant availability) produces lower coating mass with $M_{\text{R,bulk}}$ increasing from a value of about 1.0 roughly 15 minutes after the beginning of H₂SO₄ generation, to 1.2 about 3 hours later. Conversely, the H₂SO₄-high conditions (higher OH availability) lead $M_{\text{R,bulk}}$ to a quick rise to around 2.0-2.2 and a continuous increase to 3.5-3.9. The continued accumulation of coating material on soot induces a progressive increase in absorption (Fig. 1c-d). The E_{abs} values at 630 nm average at a maximum of around 1.3-1.4 (Fig. 1d), with values at 450 nm exceeding 1.5 (Fig. S2).

The retrieved average D_{fm} is within 1.89 and 2.01, and remains comparable with the value for fresh soot, indicating minimal changes to the shape of the lacy fractal particles after the initial coating addition. Nonetheless, TEM images depicts a more heterogeneous mixing state, with both partial and fully coated particles, and both compacted and fractal-like soot (Fig. 1f; more illustrative images are shown in Fig. S4).

A decrease in E_{abs} down to about 1.0-1.3 is measured at both wavelengths after 15 hours of simulated dark ageing of the coated soot (grey area Fig. 1b-1d, Fig. S2), despite the $M_{\text{R,bulk}}$ showing no significant differences. The decrease in E_{abs} is attributed to a size reduction of the absorbing soot core, as evidenced in TEM images analysis (Fig. 1g, Fig. S4), showing significant particles' restructuration. This restructuration is assumed to be caused by the continued accumulation of coating on the soot by condensation and coagulation, which homogenises the soot core structure while the $M_{\text{R,bulk}}$ remains relatively unchanged. This continuous coating formation is supported by a slight observed increase of both CMD and ρ_{eff} (Fig. 3b), and a decrease in residual O₃ and soot number concentration.

300



305

Table 2. Physico-chemical and optical properties of the fresh and the coated soot aerosol. The given properties of the fresh soot are retrieved in Heuser et al. (2025) and corresponds to soot after 60 min in suspension in the CESAM chamber. The properties of the coated soot aerosols are given at two stages: the *coated*, representing the average of soot properties between 15 and 240 minutes after coating formation, and the *aged*, representing the coated soot properties averaged between 1000 and 1300 min after coating formation, i.e. after the long-term ageing. The average and standard deviation of the bulk coating-to-soot mass ratio ($M_{R,bulk}$) and the absorption enhancement (E_{abs}) at 450 and 630 nm wavelengths are provided. The mobility exponent (D_{fm}) values are reported for the *coated* soot.

Fresh soot aerosol (Heuser et al., 2025)					
		CMD (nm)	D_{fm}	MAC ($m^2 g^{-1}$)	
				450 nm	630 nm
		145 ± 12	2.11 ± 0.04	6.0 ± 1.0	4.3 ± 0.7
Coated soot aerosol (this work)					
		$M_{R,bulk}$	D_{fm}	E_{abs}	
				450 nm	630 nm
H_2SO_4 -low	<i>Coated</i>	1.1 ± 0.1	2.01 ± 0.04	1.12 ± 0.15	1.05 ± 0.03
	<i>Aged</i>	/	/	/	/
H_2SO_4 -high1	<i>Coated</i>	2.9 ± 0.4	1.89 ± 0.06	1.41 ± 0.18	1.26 ± 0.11
	<i>Aged</i>	3.3 ± 0.4	/	1.02 ± 0.11	1.10 ± 0.09
H_2SO_4 -high2	<i>Coated</i>	2.6 ± 0.4	1.92 ± 0.06	1.37 ± 0.15	1.29 ± 0.13
	<i>Aged</i>	3.5 ± 0.9	/	1.08 ± 0.2	1.23 ± 0.13
SOA- S_{ref}	<i>Coated</i>	1.2 ± 0.1	2.24 ± 0.10	1.19 ± 0.05	1.17 ± 0.04
	<i>Aged</i>	0.5 ± 0.1	/	0.83 ± 0.04	0.85 ± 0.14
SOA $_{high}$ - S_{high}	<i>Coated</i>	1.3 ± 0.2	2.06 ± 0.08	1.31 ± 0.03	1.30 ± 0.03
	<i>Aged</i>	0.4 ± 0.1	/	1.00 ± 0.03	1.04 ± 0.03
SOA- S_{low}	<i>Coated</i>	3.3 ± 0.2	2.61 ± 0.08	1.32 ± 0.15	1.30 ± 0.08
	<i>Aged</i>	/	/	/	/

3.3 Soot-SOA coating and ageing

310

In contrast with the slower H_2SO_4 experiments, the injection of the α -pinene precursor in the O_3 -rich chamber leads to a quasi-instantaneous start of the SOA generation marked by a rapid appearance and growth of a mode below 100 nm mobility diameter associated with new particle formation (Fig. 2a, ρ_{eff} data Fig. 3c). The start of the SOA generation also marks an increase of $M_{R,bulk}$ due to the condensation of coating material on the soot particles (Fig. 2c), supported by a ρ_{eff} increase in the soot containing fraction above 100 nm diameter. The $M_{R,bulk}$ rapidly reaches an average value of around 3.3 for SOA- S_{low} (experiments with the highest precursor-to-soot-ratio), and of 1.2 to 1.3 for the SOA- S_{ref} (initial soot mass comparable to H_2SO_4 experiments) and SOA $_{high}$ - S_{high} experiments (about twice the soot and precursor concentration than SOA- S_{ref}). The D_{fm} rises to 2.06 ± 0.04 (SOA $_{high}$ - S_{high}), 2.24 ± 0.05 (SOA- S_{ref}), and 2.61 ± 0.04 (SOA- S_{low}), indicating a progressive change in the particle shape towards more spherical and compacted particles. This can be explained by the coating-induced restructuring of the soot, which is also captured in the CMD decrease for SOA- S_{ref} and SOA $_{high}$ - S_{high} , contrasted by the CMD increase for SOA- S_{low} . The TEM images show that the majority

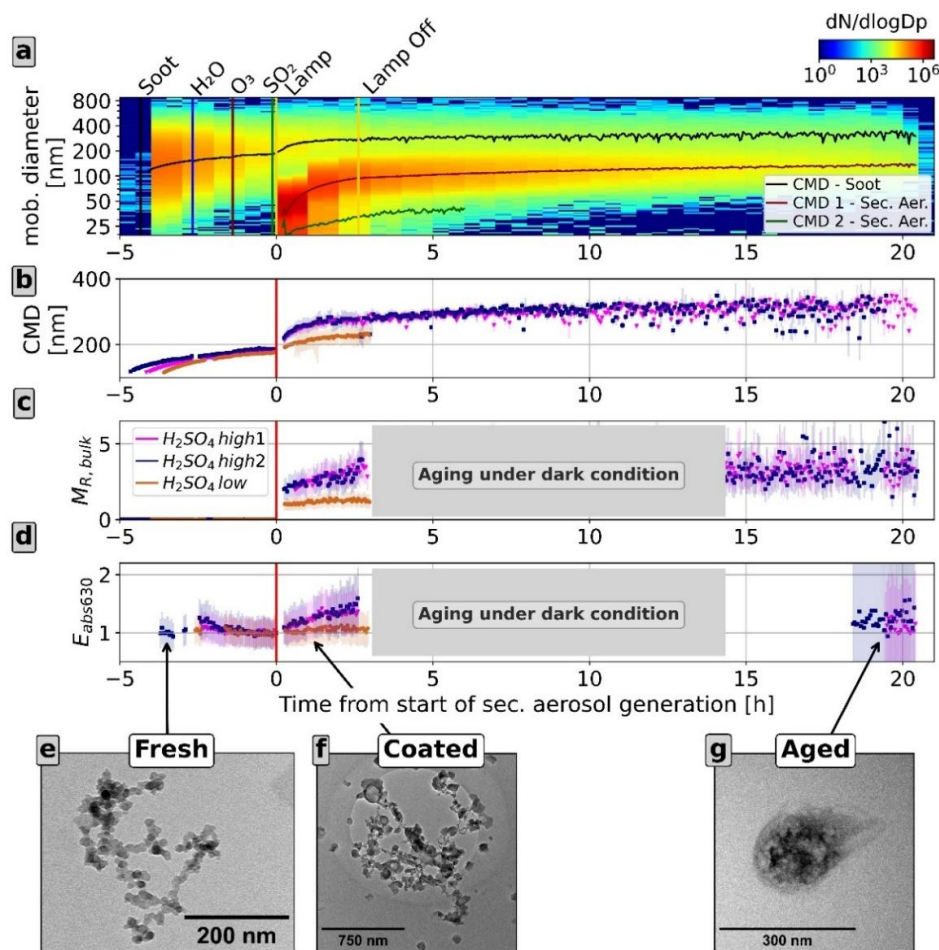
320

of soot collapsed to form small and compact aggregates (Fig. 2f-g; more illustrative images in Fig. S5), and, when visible from microscopy, the coating is identified to encapsulate soot particles. This indicates that the soot in all experiments underwent restructuring but for SOA- S_{low} it is superposed by larger coating deposition (Fig. 2b, Fig. S3). After this initial evolution, the soot



CMD for SOA-S_{ref} and SOA_{high}-S_{high} stabilizes as a consequence of minimal further SOA deposition (α -pinene precursor consumed) and negligible coagulation (as discussed in Text S2, Fig. S10). In contrast, for SOA-S_{low} the CMD of the soot peak is found to continuously decrease, interpreted as ongoing restructuring.

The E_{abs} measured at 450 and 630 nm rapidly rises following $M_{R,bulk}$ as the SOA coating on soot establishes. Then, until the aging, it remains rather stable at values between 1.2 and 1.4 for SOA-S_{ref} (Fig. 2d) and SOA_{high}-S_{high}. Higher E_{abs} up to 2 are measured for SOA-S_{low} right after coating starts due to larger $M_{R,bulk}$, decreasing afterwards following the CMD decrease and its underlying restructuring (Fig. S3).



330

335

Figure 1. (A): Time evolution of number size distribution as a function of the mobility diameter for the H₂SO₄-high1 experiment (t=0 is the start of the secondary aerosol generation). The evolution of the count median diameters (CMD) of identified modes determined from log-normal fits of the size distribution is overlaid (soot: black, H₂SO₄: red, green). Vertical lines indicate the occurrence of various events during the experiment (injection of soot, water vapour, O₃, SO₂; start and stop of irradiation, indicated as lamp on and lamp off). Time evolution of the (B) count median diameter (CMD) of the soot peak mode, (C) bulk coating-to-soot mass ratio $M_{R,bulk}$, (D) absorption enhancement factor at 630 nm for the H₂SO₄-high1, H₂SO₄-high2 and H₂SO₄-low experiments. (E, F, G): Illustrative TEM pictures for the fresh, coated, and aged soot particles from the H₂SO₄-high1 experiment. Error bars are omitted for clarity.



After 15 hours of aging in the dark, a significant decrease of $M_{R,bulk}$ and E_{abs} (0.83-1.04) at rather constant CMD is observed for the SOA- S_{ref} and SOA $_{high}$ - S_{high} experiments. The reduction of $M_{R,bulk}$, concurrently with the absence of further SOA production, negligible coagulation, invariance of CMD, and a slight reduction in the soot density, indicates a loss of coating mass on the particles. Such a loss can occur during the continuous dilution of the chamber volume, despite minimal, which can lead to the evaporation of some of the more volatile compounds of the SOA (Grieshop et al., 2007), while low-volatile organics remain on the soot and continue to affect the absorption (Zhang et al., 2023). Such a loss of coating may cause further compaction of the soot (Corbin et al., 2023), as TEM pictures show dominantly collapsed particles (Fig. 2g).

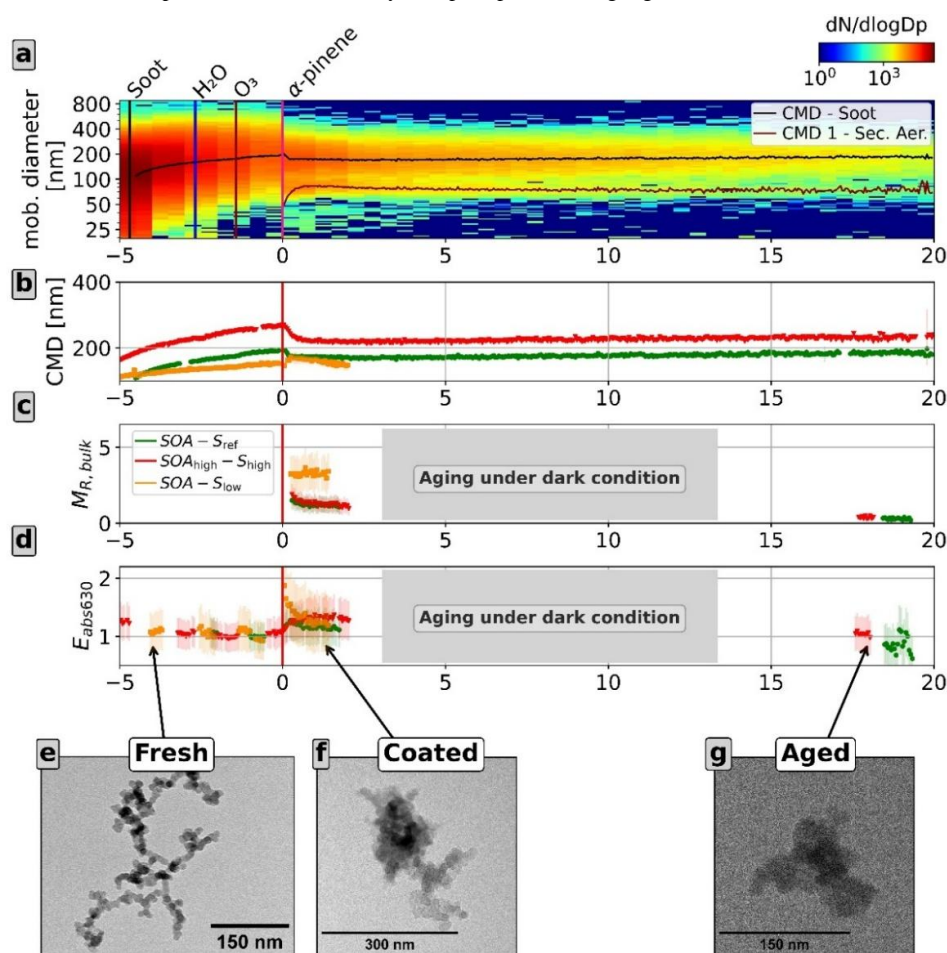
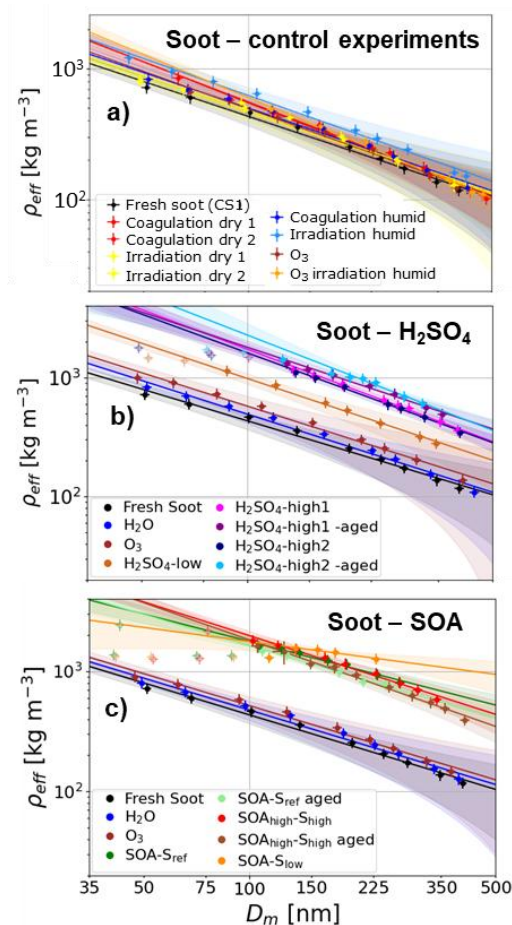


Figure 2. (A): Time evolution of number size distribution as a function of the mobility diameter for the SOA- S_{ref} coating experiment ($t=0$ is the start of the secondary aerosol generation). The evolution of the count median diameter (CMD) of different identified modes determined from log-normal fits of the size distribution is shown (soot: black, SOA: red). Vertical lines indicate the occurrence of various events during the experiments (injection of soot, water vapour, O₃, and α -pinene). Time evolution of the (B) count median diameter (CMD) of the soot peak mode, (C) bulk coating-to-soot mass ratio $M_{R,bulk}$, (D) absorption enhancement factor at 630 nm for the SOA- S_{ref} , SOA $_{high}$ - S_{high} , and SOA- S_{low} experiments. (E, F, G): Illustrative TEM pictures for the fresh, coated, and aged soot particles from the SOA- S_{ref} experiment. Error bars are omitted for clarity.



355

Figure 3. Effective density measured as a function of the mobility diameter, $\rho_{\text{eff}}(D_m)$, for (a) the different control experiments, and for (b) the H_2SO_4 and (c) the α -pinene SOA coating experiments. The power-law fits of $\rho_{\text{eff}}(D_m)$ based on Eq. 1 (coloured lines) and the fitting uncertainties (coloured-shaded areas) are shown. As a reference, the measurements for fresh soot are shown in (a). Additional plots of $\rho_{\text{eff}}(D_m)$ for the coating experiments are provided in Fig. S8. Error bars on single data points are omitted for clarity.

360

4. Discussion

4.1 Impact of coating dynamics and morphological restructuring on E_{abs}

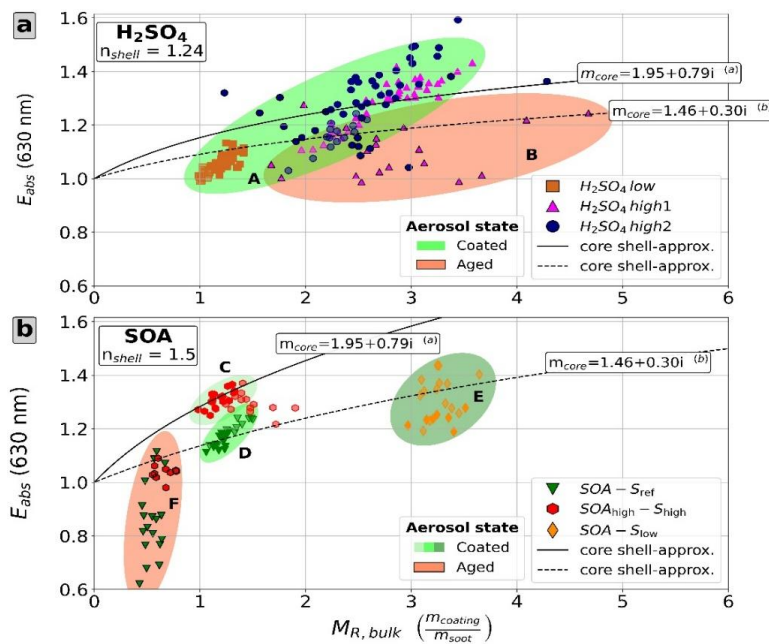
The results presented in this work evidence that E_{abs} depends not only on the quantity of coating material deposited on the soot, but also on size and morphological modifications that affect E_{abs} magnitude and evolution, modulated by different coating dynamics and aging.

365

In the experiments, larger E_{abs} are observed when aggregate shapes are more widespread and lacy aggregates are present. On the contrary, lower E_{abs} for given $M_{\text{R,bulk}}$ are measured for all conditions with more compacted soot aggregates. This is especially



prominent when comparing the clusters of the observations of SOA- S_{ref} and SOA $_{high}$ - S_{high} and can be explained by the collapse of the soot aggregate, reducing particle size and optical absorption cross section (Kahnert and Devasthale, 2011) while the coating mass remains constant. Morphological restructuring is observed both directly at the early stages of the SOA coating and for aged H₂SO₄-coated soot, indicating that E_{abs} can evolve further after an initial coating formation. This size effect can be strong enough to reduce the E_{abs} to values lower than the pre-coating state (<1) even with light coatings, as for aged SOA-coated soot. The shape, i.e. restructuring of the particles, and the coating distribution are found to vary with experiments and ageing time. The slower production of H₂SO₄ impacts the shape and thus the morphology of the soot less in the initial coating formation stages than the much faster SOA formation, which rapidly reduces mobility diameter and compacts soot particles. Only after long term ageing, the majority of particles for H₂SO₄ experiments is restructured, accompanied by a reduced E_{abs} for the aged and collapsed H₂SO₄-coated soot. Based on previous flow reactor-type measurements observing soot compaction during rapid H₂SO₄ condensation (Khalizov et al., 2009b; Zhang et al., 2008), it can be assumed that the difference is not purely compound-related but likely a result of the dynamics of the coating formation.



380 **Figure 4.** Absorption enhancement factor (E_{abs}) at 630 nm as a function of the coating-soot mass ratio ($M_{R,bulk}$) for (A) the H₂SO₄ and (B) the α -pinene SOA coating experiments. Symbols and color separate the measured data of different experiments. Slightly transparent values are measured during the initial 60 and points with black edges are taken after the ageing. Groupings of pre- (green) and post-ageing (red) values are manually highlighted using coloured ellipses. Additionally, the theoretical calculations using the Mie core-shell approximation for the different coating types are shown. The EF-core-shell curves are shown for the value of the real part corresponding to the refractive index associated to the coating material: a value of $n_{shell}=1.5$ for the SOA and $n_{shell}=1.24$ for H₂SO₄. The refractive index of the soot core (n_{core}) is set at a) $1.95 - 0.79i$, representative of BC based on Bond and Bergstrom (2006), and at b) $1.46-0.3i$ (Habib and Vervisch, 1988), representing a value on the other end of the refractive index range associated with soot. Error bars are omitted for clarity. A version of this figure including error bars is shown in Fig. S7.



4.2 Misprediction of the absorption enhancement by core-shell and fixed E_{abs} assumption

Experimental observations suggest that the E_{abs} can be significantly mispredicted if restructuring and size changes are not taken into account, a process frequently observed in ambient observations (Colbeck et al., 1990; Corbin et al., 2023; Fierce et al., 2020; Khalizov et al., 2009a; Wang et al., 2023). However, this is not possible with the commonly used idealized Mie calculations, as they rely on volumetric-based sizing, nor with fixed E_{abs} approximation. Implications of this drawback are visualized in Fig. 4 (630 nm) and Fig. S6 (450 nm), which each contain two predictions of the $E_{\text{abs}} - M_{\text{R,bulk}}$ relation based on Mie core-shell calculations for each of the two coating types. The calculated curves differ in the refractive index assumptions for the soot core, which was selected to represent both pure BC and soot, as well as values with contrasting real and imaginary components. The effect of changes in morphology is best shown in the SOA results (Fig. 4b), where clusters of E_{abs} at the same $M_{\text{R,bulk}}$ can be observed. These can be described as core-shell by varying the refractive index, even though neither the soot's nor the coating's intrinsic optical properties change between experiments. The cases for which the modelled E_{abs} align more closely with measured ones are conditions with freshly well-established coatings. While for SOA they happen instantly, for H_2SO_4 , this only applies for conditions with higher $M_{\text{R,bulk}}$ ($2 < M_{\text{R,bulk}} < 3.5$). This is in line with the observations of Liu et al. (2017) showing that a sufficient enhancement is only possible when a certain mixing ratio or threshold is reached. In this case, a core-shell internal mixing approximation may be potentially suitable for describing it. Observations from this study show that, in the range of $M_{\text{R,bulk}}$ investigated, the core-shell approximation fails to predict E_{abs} for the other conditions, i.e., uncollapsed partially coated soot with significant particle-to-particle heterogeneity and aged coated particles. Previous works using both models and experimental studies have shown that the distribution of the coating and position of the soot in the coated particles (ex., partial coating, embedded soot) can have a significant impact on the absorption enhancement and that the shape of the particle can influence this distribution (Adachi et al., 2010; Fierce et al., 2016, 2020; Liu et al., 2017; Zhang et al., 2025). Adachi et al. (2010) noted relevant inhomogeneity in particle-coating mixing, particularly for elongated non-collapsed particles. Such an inhomogeneity is likely the cause of the systematic differences between the observed and core-shell predicted E_{abs} , in particular during a slow coating generation.

Compared to experimental observations, the E_{abs} predictions at 630 nm overestimate absorption by up to 60% in the Mie-based retrieval, and by up to 40% for the, commonly used, fixed E_{abs} value of 1.5, but increasing up to 75% for fresh partial coatings or soot that has undergone restructuring. Experimental conditions characterized by established coating and only limited soot restructuring exhibit improved agreement between predicted and measured E_{abs} values, although underestimations between 2% and 30% persist.

5 Implications on radiative forcing estimations

The inability of the Mie core-shell and fixed 1.5 value to systematically predict E_{abs} has consequences for the estimates of the single scattering albedo (SSA, ratio of scattering to extinction) and radiative forcing (RF) for BC-containing aerosols. An illustrative example is given in Table 3 reporting the differences in estimated and measured SSA and the resulting relative differences in RF at 630 nm, for two assumed surface albedo. The SSA in Table 3 was estimated from Mie core-shell theory ($\text{SSA}_{\text{MieCS}}$) assuming the same complex refractive indices and particle representation as described in Sect. 2.3.2, or by assuming a fixed E_{abs} of 1.5 ($\text{SSA}_{\text{fixed-1.5}}$). To note that in the case of fixed E_{abs} , only the impact of the coating on absorption is considered for the calculation of $\text{SSA}_{\text{fixed-1.5}}$, while scattering is assumed unchanged. These values were compared to the measured SSA during



experiments (SSA_{meas}). The signal by the SOA and H_2SO_4 nucleating modes was subtracted from the total scattering and extinction when calculating SSA_{meas} . Further details on the SSA calculations are provided in Text S3.

The calculated and measured SSA values were then used to determine the change in RF by utilizing the following equation (Haywood and Shine, 1995), providing the instantaneous forcing for a thin layer of absorbing aerosols at the top-of-atmosphere:

$$430 \quad RF = -DS_0T_{at}^2(1 - A_c)SSA\beta\delta\left\{(1 - R_s)^2 - \left(\frac{2R_s}{\beta}\right)\left[\left(\frac{1}{SSA}\right) - 1\right]\right\} \quad (4)$$

where D is the fractional day length, S_0 the solar constant, T_{at} the atmospheric transmission, A_c the fractional cloud amount, SSA the aerosol single scattering albedo, β the aerosol upscatter fraction of scattering, δ the aerosol optical depth, and R_s the surface reflectivity. Despite Eq. (4) provides a simplistic estimate of RF considering only aerosol-radiation interactions and not accounting for changes compared to pre-industrial conditions, it can be used to quantify the impact of E_{abs} mispredictions on BC radiative effect. The relative change of RF due to a change from SSA_{meas} and SSA_{MieCS} (or $SSA_{fixed-1.5}$) was determined as:

$$435 \quad \Delta RF = \frac{RF_{SSAMieCS}}{RF_{SSAmeas}} = \frac{SSA_{MieCS}\left\{(1 - R_s)^2 - \left(\frac{2R_s}{\beta}\right)\left[\left(\frac{1}{SSA_{MieCS}}\right) - 1\right]\right\}}{SSA_{meas}\left\{(1 - R_s)^2 - \left(\frac{2R_s}{\beta}\right)\left[\left(\frac{1}{SSA_{meas}}\right) - 1\right]\right\}} \quad (5)$$

For Eq. (5) two values of R_s (0.2, bare soil, and 0.7, snow/ice) were used as exemplary values. The upscatter fraction β was calculated from a backscattering ratio of 0.27, determined from experimental data using the equations in Moosmüller and Ogren (2017). Calculations for SSA and RF were performed by separating data for fresh coatings (up to 1 hour from the onset of secondary aerosol formation), established coatings (second and third hour), and aged coatings (more than 15 hours).

The results in Table 3 show that for conditions that are associated with collapsed soot (H_2SO_4 -aged and SOA), the core-shell calculations underestimate the SSA on average between 12 and 56% for early, medium, and latter stages of processing. This underestimation results in an overestimation of the RF averaging at around 46%, but reaching up to 84%, for a bare soil scenario ($R_s = 0.2$), when compared to RF estimates based on SSA_{meas} . For processing stages where coatings are forming and/or the soot undergoes limited restructuring SSA values are generally found to be overestimated by 2 to 122%. This indicates that not only is the E_{abs} overestimated by the Mie-based calculations for these conditions, but so is the scattering. These SSA overpredictions lead to an average underestimation of RF of about 17% for the different stages of the experiments in a bare soil scenario. The impact of the SSA missprediction on the RF reduces with increasing surface albedo, being about 20% (collapsed soot) and 10% (inhomogeneous coating and non-collapsed soot) for a surface albedo of 0.7 associated with fresh snow.

The common alternative of a fixed E_{abs} of 1.5 leads to similar SSA and RF mispredictions. Compared to the observations, the SSA at 630 nm is consistently underestimated, in turn leading to an RF overestimation ranging between 6 and 58% in the bare soil and between 4 and 20% for the snow scenario.

455



460

Table 3. Average values of the single scattering albedo measured (SSA_{meas}) and calculated at 630 nm based on the Mie core-shell approach (SSA_{MieCS}) for two refractive indices of the soot core (n_{core}) set at 1.95 – 0.79i (Bond and Bergstrom, 2006), and 1.46-0.3i (Habib and Vervisch, 1988) and for fixed E_{abs} of 1.5 ($SSA_{fixed-1.5}$). The corresponding associated fractional change in radiative forcing, ΔRF , at 630 nm due to the SSA change is reported for varying aerosol processing states of the performed experiments. Data corresponds to a surface albedo (R_s) of 0.2 and 0.7.

Experiment	Time after coating generation [min]	SSA_{meas} measured	SSA_{MieCS} calculated MieCS (1.95-0.79i)	SSA_{MieCS} calculated MieCS (1.46-0.3i)	$SSA_{fixed-1.5}$ calculated $E_{abs}=1.5$	ΔRF					
						MieCS (1.95-0.79i)		MieCS (1.46-0.3i)		$E_{abs}=1.5$	
						R_s 0.2	R_s 0.7	R_s 0.2	R_s 0.7	R_s 0.2	R_s 0.7
H₂SO₄-high1	15 to 60 (coated)	0.18	0.29	0.30	0.13	0.79	0.87	0.75	0.85	1.11	1.07
	60 to 240 (coated)	0.28	0.31	0.36	0.21	0.93	0.96	0.79	0.88	1.20	1.11
	>1000 (aged)	0.35	0.31	0.36	0.27	1.14	1.07	0.97	0.98	1.27	1.13
H₂SO₄-high2	15 to 60 (coated)	0.17	0.29	0.31	0.12	0.77	0.86	0.72	0.83	1.10	1.06
	60 to 240 (coated)	0.30	0.30	0.35	0.22	0.98	0.99	0.86	0.92	1.21	1.11
	>1000 (aged)	0.38	0.29	0.32	0.29	1.34	1.16	1.25	1.12	1.32	1.15
H₂SO₄-low	15 to 60 (coated)	0.11	0.24	0.20	0.08	0.76	0.85	0.83	0.89	1.06	1.04
	60 to 240 (coated)	0.16	0.25	0.22	0.11	0.82	0.89	0.88	0.93	1.09	1.06
SOA-S_{ref}	15 to 60 (coated)	0.37	0.26	0.22	0.28	1.37	1.17	1.50	1.24	1.31	1.14
	60 to 240 (coated)	0.39	0.26	0.21	0.30	1.47	1.22	1.63	1.29	1.33	1.15
	>1000 (aged)	0.35	0.23	0.16	0.27	1.40	1.20	1.62	1.30	1.28	1.14
SOA_{high}-S_{high}	15 to 60 (coated)	0.33	0.27	0.24	0.25	1.19	1.09	1.29	1.14	1.25	1.13
	60 to 240 (coated)	0.37	0.26	0.21	0.28	1.39	1.18	1.54	1.26	1.31	1.15
	>1000 (aged)	0.35	0.22	0.15	0.26	1.40	1.20	1.63	1.31	1.28	1.14
SOA-S_{low}	15 to 60 (coated)	0.49	0.34	0.39	0.39	1.84	1.29	1.58	1.20	1.58	1.20
	60 to 240 (coated)	0.48	0.34	0.39	0.38	1.74	1.27	1.50	1.18	1.55	1.20

6 Summary and concluding remarks

465

This study provides a laboratory-based investigation to advance the mechanistic understanding of E_{abs} and its variability. Taking advantage of the long aerosol lifetime in the CESAM chamber, experiments were designed to explore the relationship between E_{abs} and $M_{R,bulk}$ across a variety of atmospherically relevant processes. The range of E_{abs} observed in this study for polydispersed soot under varying coating and ageing conditions lies within laboratory observations for uniform coating on monodispersed soot (Fierce et al., 2020; Peng et al., 2016) and ambient measurements in background, suburban, and urban environments (Cappa et al., 2019;

470

Liu et al., 2017; Zeng et al., 2024). The $M_{R,bulk}$ extends up to values of 5, representing most common urban and suburban conditions



(Cappa et al., 2019; Liu et al., 2017; Zeng et al., 2024), even if values as high as 10 or more are observed in urban and suburban atmospheres and during biomass burning events (McMeeking et al., 2014; Taylor et al., 2020; Wu et al., 2020; Zeng et al., 2024). Results from the present analysis support the evidence of a correlation between E_{abs} and the coating amount on soot. We highlight, however, the ambiguity of this relation based on experimental observations with varying coating and soot properties. The measured E_{abs} and the corresponding particle physico-chemical properties confirm the impact of the morphological organization of both the soot and the coating-soot system on the E_{abs} . The controlled laboratory approach provides evidence that coating formation dynamics, coating type (non-volatile/volatile), and ageing affect the composition, morphology, and size of the soot and the coating-soot system, ultimately ruling the E_{abs} magnitude and its modifications. Based on this dependence, the range of measured E_{abs} cannot systematically be predicted by the Mie core-shell approximation or by a fixed E_{abs} value, as commonly used in models.

475
480 Improving radiative forcing predictions requires models to account for the evolution of both particle and coating properties beyond coating thickness alone, in order to capture changes in optical properties, particularly the magnitude of E_{abs} and its evolution. Additional considerations include inhomogeneities in particle coatings, which we found to depend on the coating generation process, as well as the effects of morphological organization of both soot and coatings, which influence the entire soot lifetime. In order to achieve this objective, previous studies have proposed empirical adjustments of the core-shell model to reconcile with laboratory and ambient observations. These took into account morphological effects to describe single particle mixing state (Fierce et al., 2020; Liu et al., 2017) and particle-to-particle heterogeneity in mixing state (Fierce et al., 2020; Wang et al., 2023; Zeng et al., 2024). While these empirically determined adjustments allow for an improved prediction of the E_{abs} , they are often constrained to specific cases and are limited in general applicability.

485
490 More reliable approaches can be envisaged by using more advanced spectral optical theories, such as discrete dipole approximation (DDA), T-matrix, Rayleigh–Debye–Gans for coated fractal aggregate (RDG-CFA), or others (Adachi et al., 2010; Lefevre et al., 2019; Liu et al., 2016; Zhang et al., 2017). As these require detailed information on the soot and coating properties and generally also higher computational resources, they have not found wide use in large-scale models in the past decades. However, recent studies show that progressively increasing consideration of BC mixing state and nonsphericity in models leads to more accurate estimates of BC radiative forcing (Chen et al., 2024; Fierce et al., 2025; Romshoo et al., 2024; Wang et al., 2023; Zeng et al., 2024). In line with these studies, this systematic laboratory investigation stresses the need for more sophisticated approaches than core-shell Mie or fixed E_{abs} approximation to provide accurate calculations of BC absorption enhancement. The physical, chemical, and optical datasets in this study, which are made openly available to the scientific community (all data doi are listed in Table 1), can provide support for such model developments. The experimental data (such as size, $M_{\text{R,bulk}}$, E_{abs}) can be used to test and evaluate model parameterizations, in particular optical modules, and including machine learning and neural network approaches (e.g., Beeler et al., 2026). Nonetheless, more experimental investigation is required, extending to varying chemical systems and ageing conditions. With laboratory experiments being most commonly used for such mechanistic studies, we advise that setups which simulate BC coating formation under very rapid dynamics (such as flow tubes or simulation chambers considering short ageing times) should be used with care, as these approaches may produce overly idealised observations.

495
500



505 **Open Research / Data availability**

The CESAM data used in this study are available through the Database of Atmospheric Simulation Chamber Studies (DASCS) of the EUROCHAMP Data Centre (<https://data.eurochamp.org/data-access/chamber-experiments/>, last access: 20 January 2026) also available via the ACTRIS data portal (<https://data.actris.eu/>, last access: 31 March 2026) with the identifiers listed in Table 1. The core-shell optical calculations were performed with PyMieScatt, which is available at <https://github.com/bsumlin/PyMieScatt> (last access: 31 March 2026).

Competing interests

The authors declare that they have no competing interests.

Author contributions

CDB and JFD conceived the study. JH, CDB, and JFD designed the experiments and discussed the results. JH conducted the experiments with contributions by CDB, JY, MC, AB, EP, MZ, LR, AM, CY, SC, PL, MM, PF, BPV, and JFD. MM and DF performed transmission microscopy measurements. JH performed the full data analysis under the supervision of CDB and JFD and with contributions from JY, MZ, LR, AM, CY, MC, and DF. BPV, as PI of the CESAM facility, contributed to full experiment realization and management. PL provided the SP2 used in the experiments. JY provided the CPMA used in the experiments. CDB provided funding acquisition and project administration. JH, CDB, and JFD wrote the manuscript. All authors reviewed and commented on the paper.

Acknowledgements

The CNRS-INSU is gratefully acknowledged for supporting the CESAM chamber as a national facility included in the ACTRIS-France Research Infrastructure, as well as AERIS (<https://www.aeris-data.fr/>, last access: 31 March 2026) for curing and distributing the data through the EUROCHAMP Data Centre (<https://data.eurochamp.org/>, last access: 31 March 2026). Patrick Ginot is acknowledged for logistic support with SP2 operations. Contributions by Patrick Ausset, Mouad Essani, Gael Noyalet, Vera Bernardoni, Dario Massabò, Federico Mazzei, Gael Noyalet, Brice Temime-Roussel, Roberta Vecchi, and Virginia Vernocchi to experimental activities are gratefully acknowledged.

Funding

This study has been supported by the French National Research Agency (ANR) through the B2C project (contract ANR-19-CE01-0024-01), by the French National program LEFE-CHAT (Les Enveloppes Fluides et l'Environnement – Chimie Atmosphérique) through the BACON project. This work has received funding from the TNA activity of the European Union's Horizon 2020 research and innovation programme through the EUROCHAMP-2020 Infrastructure Activity under grant agreement No 730997. It has also been supported by DIM Qi² and Paris Ile-de-France Region. L. Renzi and M. Zanatta were partially supported by ITINERIS project (IR0000032), the Italian Integrated Environmental Research Infrastructures System (D.D. n. 130/2022 - CUP B53C22002150006), funded by EU - Next Generation EU PNRR- Mission 4 "Education and Research".



References

- Adachi, K., Chung, S. H., and Buseck, P. R.: Shapes of soot aerosol particles and implications for their effects on climate, *J. Geophys. Res.*, 115, 2009JD012868, <https://doi.org/10.1029/2009JD012868>, 2010.
- 540 Anderson, T. L., Covert, D. S., Marshall, S. F., Laucks, M. L., Charlson, R. J., Waggoner, A. P., Ogren, J. A., Caldow, R., Holm, R. L., Quant, F. R., Sem, G. J., Wiedensohler, A., Ahlquist, N. A., and Bates, T. S.: Performance Characteristics of a High-Sensitivity, Three-Wavelength, Total Scatter/Backscatter Nephelometer, *Journal of Atmospheric and Oceanic Technology*, 13, 967–986, [https://doi.org/10.1175/1520-0426\(1996\)013%3C0967:PCOAHS%3E2.0.CO;2](https://doi.org/10.1175/1520-0426(1996)013%3C0967:PCOAHS%3E2.0.CO;2), 1996.
- 545 Asmi, E., Sipkens, T. A., Saturno, J., Backman, J., Vasilatou, K., Weingartner, E., Keller, A., Ciupek, K., Müller, T., Babu Suja, A., Močnik, G., Drinovec, L., Eleftheriadis, K., Gini, M. I., Nowak, A., and Corbin, J. C.: Mass absorption cross-section of ambient black carbon aerosols - a review, *npj Clim Atmos Sci*, 9, 17, <https://doi.org/10.1038/s41612-025-01288-2>, 2025.
- Baldo, C., Formenti, P., Nowak, S., Chevaillier, S., Cazaunau, M., Pangui, E., Di Biagio, C., Doussin, J.-F., Ignatyev, K., Dagsson-Waldhauserova, P., Arnalds, O., MacKenzie, A. R., and Shi, Z.: Distinct chemical and mineralogical composition of Icelandic dust compared to northern African and Asian dust, *Atmospheric Chemistry and Physics*, 20, 13521–13539, <https://doi.org/10.5194/acp-20-13521-2020>, 2020.
- 550 Baldo, C., Formenti, P., Di Biagio, C., Lu, G., Song, C., Cazaunau, M., Pangui, E., Doussin, J.-F., Dagsson-Waldhauserova, P., Arnalds, O., Beddows, D., MacKenzie, A. R., and Shi, Z.: Complex refractive index and single scattering albedo of Icelandic dust in the shortwave spectrum, *EGUsphere*, 2023, 1–42, <https://doi.org/10.5194/egusphere-2023-276>, 2023.
- 555 Battaglia, F., Formenti, P., Giorio, C., Cazaunau, M., Pangui, E., Bergé, A., Gratien, A., Pereira, D. L., Bertin, T., de Brito, J. F., Romanias, M. N., Michoud, V., Baldo, C., Chevaillier, S., Noyalet, G., Decorse, P., Picquet-Varrault, B., and Doussin, J.-F.: Formation and composition of organic aerosols from the uptake of glyoxal on natural mineral dust aerosols: a laboratory study, *Atmospheric Chemistry and Physics*, 25, 12409–12431, <https://doi.org/10.5194/acp-25-12409-2025>, 2025.
- Beeler, P., Donald, S., and Fierce, L.: DDA-BNN v1.0: A Morphology-Aware Surrogate Model for the Optical Properties of Black Carbon–Containing Particles, *EGUsphere*, 1–27, <https://doi.org/10.5194/egusphere-2026-1270>, 2026.
- 560 Bond, T. C. and Bergstrom, R. W.: Light Absorption by Carbonaceous Particles: An Investigative Review, *Aerosol Science and Technology*, 40, 27–67, <https://doi.org/10.1080/02786820500421521>, 2006.
- Bond, T. C., Doherty, S. J., Fahey, D. W., Forster, P. M., Berntsen, T., DeAngelo, B. J., Flanner, M. G., Ghan, S., Kärcher, B., Koch, D., Kinne, S., Kondo, Y., Quinn, P. K., Sarofim, M. C., Schultz, M. G., Schulz, M., Venkataraman, C., Zhang, H., Zhang, S., Bellouin, N., Guttikunda, S. K., Hopke, P. K., Jacobson, M. Z., Kaiser, J. W., Klimont, Z., Lohmann, U., Schwarz, J. P., Shindell, D., Storelvmo, T., Warren, S. G., and Zender, C. S.: Bounding the role of black carbon in the climate system: A scientific assessment: BLACK CARBON IN THE CLIMATE SYSTEM, *J. Geophys. Res. Atmos.*, 118, 5380–5552, <https://doi.org/10.1002/jgrd.50171>, 2013.
- 565 Caponi, L., Formenti, P., Massabó, D., Di Biagio, C., Cazaunau, M., Pangui, E., Chevaillier, S., Landrot, G., Andreae, M. O., Kandler, K., Piketh, S., Saeed, T., Seibert, D., Williams, E., Balkanski, Y., Prati, P., and Doussin, J.-F.: Spectral- and size-resolved mass absorption efficiency of mineral dust aerosols in the shortwave spectrum: a simulation chamber study, *Atmospheric Chemistry and Physics*, 17, 7175–7191, <https://doi.org/10.5194/acp-17-7175-2017>, 2017.
- 570 Cappa, C. D., Onasch, T. B., Massoli, P., Worsnop, D. R., Bates, T. S., Cross, E. S., Davidovits, P., Hakala, J., Hayden, K. L., Jobson, B. T., Kolesar, K. R., Lack, D. A., Lerner, B. M., Li, S.-M., Mellon, D., Nuaaman, I., Olfert, J. S., Petäjä, T., Quinn, P. K., Song, C., Subramanian, R., Williams, E. J., and Zaveri, R. A.: Radiative Absorption Enhancements Due to the Mixing State of Atmospheric Black Carbon, *Science*, 337, 1078–1081, <https://doi.org/10.1126/science.1223447>, 2012a.
- 575 Cappa, C. D., Onasch, T. B., Massoli, P., Worsnop, D. R., Bates, T. S., Cross, E. S., Davidovits, P., Hakala, J., Hayden, K. L., Jobson, B. T., Kolesar, K. R., Lack, D. A., Lerner, B. M., Li, S.-M., Mellon, D., Nuaaman, I., Olfert, J. S., Petäjä, T., Quinn, P. K., Song, C., Subramanian, R., Williams, E. J., and Zaveri, R. A.: Radiative Absorption Enhancements Due to the Mixing State of Atmospheric Black Carbon, *Science*, 337, 1078–1081, <https://doi.org/10.1126/science.1223447>, 2012b.
- 580 Cappa, C. D., Zhang, X., Russell, L. M., Collier, S., Lee, A. K. Y., Chen, C., Betha, R., Chen, S., Liu, J., Price, D. J., Sanchez, K. J., McMeeking, G. R., Williams, L. R., Onasch, T. B., Worsnop, D. R., Abbatt, J., and Zhang, Q.: Light Absorption by Ambient



Black and Brown Carbon and its Dependence on Black Carbon Coating State for Two California, USA, Cities in Winter and Summer, *JGR Atmospheres*, 124, 1550–1577, <https://doi.org/10.1029/2018JD029501>, 2019.

585 Chan, T. W., Huang, L., Leaitch, W. R., Sharma, S., Brook, J. R., Slowik, J. G., Abbatt, J. P. D., Brickell, P. C., Liggio, J., Li, S.-M., and Moosmüller, H.: Observations of OM/OC and specific attenuation coefficients (SAC) in ambient fine PM at a rural site in central Ontario, Canada, *Atmos. Chem. Phys.*, 10, 2393–2411, <https://doi.org/10.5194/acp-10-2393-2010>, 2010.

Chen, G., Liu, C., Wang, J., Yin, Y., and Wang, Y.: Accounting for Black Carbon Mixing State, Nonsphericity, and Heterogeneity Effects in Its Optical Property Parameterization in a Climate Model, *JGR Atmospheres*, 129, <https://doi.org/10.1029/2024jd041135>, 2024.

590 Cheng, Z., Atwi ,Khairallah, Onyima ,Travis, and and Saleh, R.: Investigating the dependence of light-absorption properties of combustion carbonaceous aerosols on combustion conditions, *Aerosol Science and Technology*, 53, 419–434, <https://doi.org/10.1080/02786826.2019.1566593>, 2019.

Colbeck, I., Appleby, L., Hardman, E. J., and Harrison, R. M.: The optical properties and morphology of cloud-processed carbonaceous smoke, *Journal of Aerosol Science*, 21, 527–538, [https://doi.org/10.1016/0021-8502\(90\)90129-L](https://doi.org/10.1016/0021-8502(90)90129-L), 1990.

595 Corbin, J. C., Modini, R. L., and Gysel-Beer, M.: Mechanisms of soot-aggregate restructuring and compaction, *Aerosol Science and Technology*, 57, 89–111, <https://doi.org/10.1080/02786826.2022.2137385>, 2023.

De Haan, D. O., Hawkins, L. N., Wickremasinghe, P. D., Andretta, A. D., Dignum, J. R., De Haan, A. C., Welsh, H. G., Pennington, E. A., Cui, T., Surratt, J. D., Cazaunau, M., Pangui, E., and Doussin, J.-F.: Brown Carbon from Photo-Oxidation of Glyoxal and SO₂ in Aqueous Aerosol, *ACS Earth Space Chem.*, 7, 1131–1140, <https://doi.org/10.1021/acsearthspacechem.3c00035>, 2023.

600 Denjean, C., Formenti, P., Picquet-Varrault, B., Pangui, E., Zapf, P., Katrib, Y., Giorio, C., Tapparo, A., Monod, A., Temime-Roussel, B., Decorse, P., Mangeney, C., and Doussin, J. F.: Relating hygroscopicity and optical properties to chemical composition and structure of secondary organic aerosol particles generated from the ozonolysis of α -pinene, *Atmospheric Chemistry and Physics*, 15, 3339–3358, <https://doi.org/10.5194/acp-15-3339-2015>, 2015.

605 Di Biagio, C., Formenti, P., Balkanski, Y., Caponi, L., Cazaunau, M., Pangui, E., Journet, E., Nowak, S., Caquineau, S., Andreae, M. O., Kandler, K., Saeed, T., Piketh, S., Seibert, D., Williams, E., and Doussin, J.-F.: Global scale variability of the mineral dust long-wave refractive index: a new dataset of in situ measurements for climate modeling and remote sensing, *Atmospheric Chemistry and Physics*, 17, 1901–1929, <https://doi.org/https://doi.org/10.5194/acp-17-1901-2017>, 2017.

610 Di Biagio, C., Formenti, P., Balkanski, Y., Caponi, L., Cazaunau, M., Pangui, E., Journet, E., Nowak, S., Andreae, M. O., Kandler, K., Saeed, T., Piketh, S., Seibert, D., Williams, E., and Doussin, J.-F.: Complex refractive indices and single-scattering albedo of global dust aerosols in the shortwave spectrum and relationship to size and iron content, *Atmospheric Chemistry and Physics*, 19, 15503–15531, <https://doi.org/https://doi.org/10.5194/acp-19-15503-2019>, 2019.

Di Biagio, C., Doussin, J.-F., Cazaunau, M., Pangui, E., Cuesta, J., Sellitto, P., Ródenas, M., and Formenti, P.: Infrared optical signature reveals the source-dependency and along-transport evolution of dust mineralogy as shown by laboratory study, *Scientific Reports*, 13, 13252, <https://doi.org/10.1038/s41598-023-39336-7>, 2023.

615 Doussin, J.-F., Fuchs, H., Kiendler-Scharr, A., Seakins, P., and Wenger, J. (Eds.): *A Practical Guide to Atmospheric Simulation Chambers*, Springer International Publishing, Cham, <https://doi.org/10.1007/978-3-031-22277-1>, 2023.

Fierce, L., Bond, T. C., Bauer, S. E., Mena, F., and Riemer, N.: Black carbon absorption at the global scale is affected by particle-scale diversity in composition, *Nat Commun*, 7, 12361, <https://doi.org/10.1038/ncomms12361>, 2016.

620 Fierce, L., Onasch, T. B., Cappa, C. D., Mazzoleni, C., China, S., Bhandari, J., Davidovits, P., Fischer, D. A., Helgestad, T., Lambe, A. T., Sedlacek, A. J., Smith, G. D., and Wolff, L.: Radiative absorption enhancements by black carbon controlled by particle-to-particle heterogeneity in composition, *Proc. Natl. Acad. Sci. U.S.A.*, 117, 5196–5203, <https://doi.org/10.1073/pnas.1919723117>, 2020.

Fierce, L., Li, Y., Feng, Y., Riemer, N., Schutgens, N. A. J., Aiken, A. C., Dubey, M. K., Ma, P., and Wuebbles, D.: Constraining Black Carbon Aging in Global Models to Reflect Timescales for Internal Mixing, *J Adv Model Earth Syst*, 17, <https://doi.org/10.1029/2024ms004471>, 2025.



- 625 Fuller, K. A., Malm, W. C., and Kreidenweis, S. M.: Effects of mixing on extinction by carbonaceous particles, *J. Geophys. Res.*, 104, 15941–15954, <https://doi.org/10.1029/1998JD100069>, 1999.
- Grieshop, A. P., Donahue, N. M., and Robinson, A. L.: Is the gas-particle partitioning in alpha-pinene secondary organic aerosol reversible?, *Geophysical Research Letters*, 34, 2007GL029987, <https://doi.org/10.1029/2007GL029987>, 2007.
- 630 Habib, Z. G. and Vervisch, P.: On The Refractive Index of Soot at Flame Temperature, *Combustion Science and Technology*, 59, 261–274, <https://doi.org/10.1080/00102208808947100>, 1988.
- Haywood, J. M. and Shine, K. P.: The effect of anthropogenic sulfate and soot aerosol on the clear sky planetary radiation budget, *Geophysical Research Letters*, 22, 603–606, <https://doi.org/10.1029/95GL00075>, 1995.
- 635 Healy, R. M., Wang, J. M., Jeong, C. -H., Lee, A. K. Y., Willis, M. D., Jaroudi, E., Zimmerman, N., Hilker, N., Murphy, M., Eckhardt, S., Stohl, A., Abbatt, J. P. D., Wenger, J. C., and Evans, G. J.: Light-absorbing properties of ambient black carbon and brown carbon from fossil fuel and biomass burning sources, *JGR Atmospheres*, 120, 6619–6633, <https://doi.org/10.1002/2015JD023382>, 2015.
- 640 Heuser, J., Di Biagio, C., Yon, J., Cazaunau, M., Bergé, A., Pangui, E., Zanatta, M., Renzi, L., Marinoni, A., Inomata, S., Yu, C., Bernardoni, V., Chevaillier, S., Ferry, D., Laj, P., Maillé, M., Massabò, D., Mazzei, F., Noyalet, G., Tanimoto, H., Temime-Roussel, B., Vecchi, R., Vernocchi, V., Formenti, P., Picquet-Varrault, B., and Doussin, J.-F.: Spectral optical properties of soot: laboratory investigation of propane flame particles and their link to composition, *Atmos. Chem. Phys.*, 25, 6407–6428, <https://doi.org/10.5194/acp-25-6407-2025>, 2025.
- Intergovernmental Panel on Climate Change (IPCC) (Ed.): Short-lived Climate Forcers, in: *Climate Change 2021 – The Physical Science Basis: Working Group I Contribution to the Sixth Assessment Report of the Intergovernmental Panel on Climate Change*, Cambridge University Press, Cambridge, 817–922, <https://doi.org/10.1017/9781009157896.008>, 2023.
- 645 Kahnert, M. and Devasthale, A.: Black carbon fractal morphology and short-wave radiative impact: a modelling study, *Atmos. Chem. Phys.*, 11, 11745–11759, <https://doi.org/10.5194/acp-11-11745-2011>, 2011.
- Kasper, G.: Dynamics and Measurement of Smokes. I Size Characterization of Nonspherical Particles, *Aerosol Science and Technology*, 1, 187–199, <https://doi.org/10.1080/02786828208958587>, 1982.
- 650 Kebabian, P. L., Robinson, W. A., and Freedman, A.: Optical extinction monitor using cw cavity enhanced detection, *Rev. Sci. Instrum.*, 78, 063102, <https://doi.org/10.1063/1.2744223>, 2007.
- Khalizov, A. F., Xue, H., Wang, L., Zheng, J., and Zhang, R.: Enhanced Light Absorption and Scattering by Carbon Soot Aerosol Internally Mixed with Sulfuric Acid, *J. Phys. Chem. A*, 113, 1066–1074, <https://doi.org/10.1021/jp807531n>, 2009a.
- 655 Khalizov, A. F., Zhang, R., Zhang, D., Xue, H., Pagels, J., and McMurry, P. H.: Formation of highly hygroscopic soot aerosols upon internal mixing with sulfuric acid vapor, *J. Geophys. Res.*, 114, 2008JD010595, <https://doi.org/10.1029/2008JD010595>, 2009b.
- Kim, H., Barkey, B., and Paulson, S. E.: Real refractive indices of α - and β -pinene and toluene secondary organic aerosols generated from ozonolysis and photo-oxidation, *Journal of Geophysical Research: Atmospheres*, 115, <https://doi.org/10.1029/2010JD014549>, 2010.
- 660 Laborde, M., Schnaiter, M., Linke, C., Saathoff, H., Naumann, K.-H., Möhler, O., Berlenz, S., Wagner, U., Taylor, J. W., Liu, D., Flynn, M., Allan, J. D., Coe, H., Heimerl, K., Dahlkötter, F., Weinzierl, B., Wollny, A. G., Zanatta, M., Cozic, J., Laj, P., Hittenberger, R., Schwarz, J. P., and Gysel, M.: Single Particle Soot Photometer intercomparison at the AIDA chamber, *Atmos. Meas. Tech.*, 5, 3077–3097, <https://doi.org/10.5194/amt-5-3077-2012>, 2012.
- 665 Lack, D. A., Cappa, C. D., Cross, E. S., Massoli, P., Ahern, A. T., Davidovits, P., and Onasch, T. B.: Absorption Enhancement of Coated Absorbing Aerosols: Validation of the Photo-Acoustic Technique for Measuring the Enhancement, *Aerosol Science and Technology*, 43, 1006–1012, <https://doi.org/10.1080/02786820903117932>, 2009.



- Lamkaddam, H., Gratien, A., Pangu, E., Cazaunau, M., Picquet-Varrault, B., and Doussin, J.-F.: High-NO_x Photooxidation of n-Dodecane: Temperature Dependence of SOA Formation, *Environ. Sci. Technol.*, 51, 192–201, <https://doi.org/10.1021/acs.est.6b03821>, 2017.
- 670 Lee, D. S., Fahey, D. W., Skowron, A., Allen, M. R., Burkhardt, U., Chen, Q., Doherty, S. J., Freeman, S., Forster, P. M., Fuglestedt, J., Gettelman, A., De León, R. R., Lim, L. L., Lund, M. T., Millar, R. J., Owen, B., Penner, J. E., Pitari, G., Prather, M. J., Sausen, R., and Wilcox, L. J.: The contribution of global aviation to anthropogenic climate forcing for 2000 to 2018, *Atmospheric Environment*, 244, 117834, <https://doi.org/10.1016/j.atmosenv.2020.117834>, 2021.
- Lefevre, G., Yon, J., Bouvier, M., Liu, F., and Coppalle, A.: Impact of Organic Coating on Soot Angular and Spectral Scattering Properties, *Environ. Sci. Technol.*, 53, 6383–6391, <https://doi.org/10.1021/acs.est.8b05482>, 2019.
- 675 Liu, D., Allan, J. D., Young, D. E., Coe, H., Beddows, D., Fleming, Z. L., Flynn, M. J., Gallagher, M. W., Harrison, R. M., Lee, J., Prevot, A. S. H., Taylor, J. W., Yin, J., Williams, P. I., and Zotter, P.: Size distribution, mixing state and source apportionment of black carbon aerosol in London during wintertime, *Atmos. Chem. Phys.*, 14, 10061–10084, <https://doi.org/10.5194/acp-14-10061-2014>, 2014.
- 680 Liu, D., Whitehead, J., Alfarra, M. R., Reyes-Villegas, E., Spracklen, D. V., Reddington, C. L., Kong, S., Williams, P. I., Ting, Y.-C., Haslett, S., Taylor, J. W., Flynn, M. J., Morgan, W. T., McFiggans, G., Coe, H., and Allan, J. D.: Black-carbon absorption enhancement in the atmosphere determined by particle mixing state, *Nature Geosci.*, 10, 184–188, <https://doi.org/10.1038/ngeo2901>, 2017.
- Liu, D., He, C., Schwarz, J. P., and Wang, X.: Lifecycle of light-absorbing carbonaceous aerosols in the atmosphere, *npj Clim Atmos Sci.*, 3, 40, <https://doi.org/10.1038/s41612-020-00145-8>, 2020.
- 685 Liu, F., Yon, J., and Bescond, A.: On the radiative properties of soot aggregates – Part 2: Effects of coating, *Journal of Quantitative Spectroscopy and Radiative Transfer*, 172, 134–145, <https://doi.org/10.1016/j.jqsrt.2015.08.005>, 2016.
- Liu, S., Aiken, A. C., Gorkowski, K., Dubey, M. K., Cappa, C. D., Williams, L. R., Herndon, S. C., Massoli, P., Fortner, E. C., Chhabra, P. S., Brooks, W. A., Onasch, T. B., Jayne, J. T., Worsnop, D. R., China, S., Sharma, N., Mazzoleni, C., Xu, L., Ng, N. L., Liu, D., Allan, J. D., Lee, J. D., Fleming, Z. L., Mohr, C., Zotter, P., Szidat, S., and Prévôt, A. S. H.: Enhanced light absorption by mixed source black and brown carbon particles in UK winter, *Nat Commun.*, 6, 8435, <https://doi.org/10.1038/ncomms9435>, 2015.
- 690 Maricq, M. M. and Xu, N.: The effective density and fractal dimension of soot particles from premixed flames and motor vehicle exhaust, *Journal of Aerosol Science*, 35, 1251–1274, <https://doi.org/10.1016/j.jaerosci.2004.05.002>, 2004.
- 695 Massoli, P., Murphy, D. M., Lack, D. A., Baynard, T., Brock, C. A., and Lovejoy, E. R.: Uncertainty in Light Scattering Measurements by TSI Nephelometer: Results from Laboratory Studies and Implications for Ambient Measurements, *Aerosol Science and Technology*, 43, 1064–1074, <https://doi.org/10.1080/02786820903156542>, 2009.
- Massoli, P., Kebedian, P. L., Onasch, T. B., Hills, F. B., and Freedman, A.: Aerosol Light Extinction Measurements by Cavity Attenuated Phase Shift (CAPS) Spectroscopy: Laboratory Validation and Field Deployment of a Compact Aerosol Particle Extinction Monitor, *Aerosol Science and Technology*, 44, 428–435, <https://doi.org/10.1080/02786821003716599>, 2010.
- 700 McMeeking, G. R., Fortner, E., Onasch, T. B., Taylor, J. W., Flynn, M., Coe, H., and Kreidenweis, S. M.: Impacts of nonrefractory material on light absorption by aerosols emitted from biomass burning, *Journal of Geophysical Research: Atmospheres*, 119, 12,272–12,286, <https://doi.org/10.1002/2014JD021750>, 2014.
- 705 Moore, R. H., Ziemba, L. D., Dutcher, D., Beyersdorf, A. J., Chan, K., Crumeyrolle, S., Raymond, T. M., Thornhill, K. L., Winstead, E. L., and Anderson, B. E.: Mapping the Operation of the Miniature Combustion Aerosol Standard (Mini-CAST) Soot Generator, *Aerosol Science and Technology*, 48, 467–479, <https://doi.org/10.1080/02786826.2014.890694>, 2014.
- Moosmüller, H. and Ogren, J. A.: Parameterization of the Aerosol Upscatter Fraction as Function of the Backscatter Fraction and Their Relationships to the Asymmetry Parameter for Radiative Transfer Calculations, *Atmosphere*, 8, 133, <https://doi.org/10.3390/atmos8080133>, 2017.



- 710 Onasch, T. B., Massoli, P., Keabian, P. L., Hills, F. B., Bacon, F. W., and Freedman, A.: Single Scattering Albedo Monitor for Airborne Particulates, *Aerosol Science and Technology*, 49, 267–279, <https://doi.org/10.1080/02786826.2015.1022248>, 2015.
- Park, K., Cao, F., Kittelson, D. B., and McMurry, P. H.: Relationship between Particle Mass and Mobility for Diesel Exhaust Particles, *Environ. Sci. Technol.*, 37, 577–583, <https://doi.org/10.1021/es025960v>, 2003.
- 715 Peng, J., Hu, M., Guo, S., Du, Z., Zheng, J., Shang, D., Levy Zamora, M., Zeng, L., Shao, M., Wu, Y.-S., Zheng, J., Wang, Y., Glen, C. R., Collins, D. R., Molina, M. J., and Zhang, R.: Markedly enhanced absorption and direct radiative forcing of black carbon under polluted urban environments, *Proc Natl Acad Sci USA*, 113, 4266–4271, <https://doi.org/10.1073/pnas.1602310113>, 2016.
- Romshoo, B., Müller, T., Ahlawat, A., Wiedensohler, A., Haneef, M. V., Imran, Mohd., Warsi, A. B., Mandariya, A. K., Habib, G., and Pöhlker, M. L.: Significant contribution of fractal morphology to aerosol light absorption in polluted environments dominated by black carbon (BC), *npj Clim Atmos Sci*, 7, 87, <https://doi.org/10.1038/s41612-024-00634-0>, 2024.
- 720 Sand, M., Samset, B. H., Myhre, G., Gliß, J., Bauer, S. E., Bian, H., Chin, M., Checa-Garcia, R., Ginoux, P., Kipling, Z., Kirkevåg, A., Kokkola, H., Le Sager, P., Lund, M. T., Matsui, H., van Noije, T., Olivie, D. J. L., Remy, S., Schulz, M., Stier, P., Stjern, C. W., Takemura, T., Tsigaridis, K., Tsyro, S. G., and Watson-Parris, D.: Aerosol absorption in global models from AeroCom phase III, *Atmospheric Chemistry and Physics*, 21, 15929–15947, <https://doi.org/10.5194/acp-21-15929-2021>, 2021.
- 725 Schnaiter, M., Linke, C., Möhler, O., Naumann, K. -H., Saathoff, H., Wagner, R., Schurath, U., and Wehner, B.: Absorption amplification of black carbon internally mixed with secondary organic aerosol, *J. Geophys. Res.*, 110, 2005JD006046, <https://doi.org/10.1029/2005JD006046>, 2005.
- 730 Schwarz, J. P., Gao, R. S., Fahey, D. W., Thomson, D. S., Watts, L. A., Wilson, J. C., Reeves, J. M., Darbeheshti, M., Baumgardner, D. G., Kok, G. L., Chung, S. H., Schulz, M., Hendricks, J., Lauer, A., Kärcher, B., Slowik, J. G., Rosenlof, K. H., Thompson, T. L., Langford, A. O., Loewenstein, M., and Aikin, K. C.: Single-particle measurements of midlatitude black carbon and light-scattering aerosols from the boundary layer to the lower stratosphere, *J. Geophys. Res.*, 111, 2006JD007076, <https://doi.org/10.1029/2006JD007076>, 2006.
- Sedlacek III, A. J., Lewis, E. R., Kleinman, L., Xu, J., and Zhang, Q.: Determination of and evidence for non-core-shell structure of particles containing black carbon using the Single-Particle Soot Photometer (SP2), *Geophysical Research Letters*, 39, <https://doi.org/10.1029/2012GL050905>, 2012.
- 735 Sorensen, C. M.: The Mobility of Fractal Aggregates: A Review, *Aerosol Science and Technology*, 45, 765–779, <https://doi.org/10.1080/02786826.2011.560909>, 2011.
- Stephens, M., Turner, N., and Sandberg, J.: Particle identification by laser-induced incandescence in a solid-state laser cavity, *Applied Optics*, Vol. 42, Issue 19, pp. 3726–3736, <https://doi.org/10.1364/AO.42.003726>, 2003.
- 740 Taylor, J. W., Wu, H., Szpek, K., Bower, K., Crawford, I., Flynn, M. J., Williams, P. I., Dorsey, J., Langridge, J. M., Cotterell, M. I., Fox, C., Davies, N. W., Haywood, J. M., and Coe, H.: Absorption closure in highly aged biomass burning smoke, *Atmospheric Chemistry and Physics*, 20, 11201–11221, <https://doi.org/10.5194/acp-20-11201-2020>, 2020.
- Wang, J., Doussin, J. F., Perrier, S., Perraudin, E., Katrib, Y., Pangu, E., and Picquet-Varrault, B.: Design of a new multi-phase experimental simulation chamber for atmospheric photochemistry, aerosol and cloud chemistry research, *Atmos. Meas. Tech.*, 4, 2465–2494, <https://doi.org/10.5194/amt-4-2465-2011>, 2011.
- 745 Wang, J., Wang, J., Cai, R., Liu, C., Jiang, J., Nie, W., Wang, J., Moteki, N., Zaveri, R. A., Huang, X., Ma, N., Chen, G., Wang, Z., Jin, Y., Cai, J., Zhang, Y., Chi, X., Holanda, B. A., Xing, J., Liu, T., Qi, X., Wang, Q., Pöhlker, C., Su, H., Cheng, Y., Wang, S., Hao, J., Andreae, M. O., and Ding, A.: Unified theoretical framework for black carbon mixing state allows greater accuracy of climate effect estimation, *Nat Commun*, 14, 2703, <https://doi.org/10.1038/s41467-023-38330-x>, 2023.
- 750 Wang, Y., Liu, F., He, C., Bi, L., Cheng, T., Wang, Z., Zhang, H., Zhang, X., Shi, Z., and Li, W.: Fractal Dimensions and Mixing Structures of Soot Particles during Atmospheric Processing, *Environ. Sci. Technol. Lett.*, 4, 487–493, <https://doi.org/10.1021/acs.estlett.7b00418>, 2017.



- Wu, Y., Cheng, T., Pan, X., Zheng, L., Shi, S., and Liu, H.: The role of biomass burning states in light absorption enhancement of carbonaceous aerosols, *Sci Rep*, 10, 12829, <https://doi.org/10.1038/s41598-020-69611-w>, 2020.
- 755 Yon, J., Bescond, A., and Ouf, F.-X.: A simple semi-empirical model for effective density measurements of fractal aggregates, *Journal of Aerosol Science*, 87, 28–37, <https://doi.org/10.1016/j.jaerosci.2015.05.003>, 2015.
- Zeng, L., Tan, T., Zhao, G., Du, Z., Hu, S., Shang, D., and Hu, M.: Overestimation of black carbon light absorption due to mixing state heterogeneity, *npj Clim Atmos Sci*, 7, 1–8, <https://doi.org/10.1038/s41612-023-00535-8>, 2024.
- 760 Zhang, R., Khalizov, A. F., Pagels, J., Zhang, D., Xue, H., and McMurry, P. H.: Variability in morphology, hygroscopicity, and optical properties of soot aerosols during atmospheric processing, *Proc. Natl. Acad. Sci. U.S.A.*, 105, 10291–10296, <https://doi.org/10.1073/pnas.0804860105>, 2008.
- Zhang, X., Mao, M., Yin, Y., and Wang, B.: Absorption enhancement of aged black carbon aerosols affected by their microphysics: A numerical investigation, *Journal of Quantitative Spectroscopy and Radiative Transfer*, 202, 90–97, <https://doi.org/10.1016/j.jqsrt.2017.07.025>, 2017.
- 765 Zhang, Y., Favez, O., Canonaco, F., Liu, D., Močnik, G., Amodeo, T., Sciare, J., Prévôt, A. S. H., Gros, V., and Albinet, A.: Evidence of major secondary organic aerosol contribution to lensing effect black carbon absorption enhancement, *npj Clim Atmos Sci*, 1, 47, <https://doi.org/10.1038/s41612-018-0056-2>, 2018.
- Zhang, Y., Su, H., Kecorius, S., Ma, N., Wang, Z., Sun, Y., Zhang, Q., Pöschl, U., Wiedensohler, A., Andreae, M. O., and Cheng, Y.: Extremely low-volatility organic coating leads to underestimation of black carbon climate impact, *One Earth*, 6, 158–166, <https://doi.org/10.1016/j.oneear.2023.01.009>, 2023.
- 770 Zhang, Z., Wang, Y., Chen, X., Xu, L., Zheng, Z., Ching, J., Zhu, S., Liu, D., and Li, W.: Absorption enhancement and shielding effect of brown organic coating on black carbon aerosols, *npj Clim Atmos Sci*, 8, 102, <https://doi.org/10.1038/s41612-025-00989-y>, 2025.